Phase Diagram of the Multi-Orbital Hubbard Model

Submitted by

Bence Temesi

BACHELOR THESIS

Faculty of Physics

at Ludwig-Maximilians-Universität München

Supervisor:

Prof. Dr. Jan von Delft

Munich, August 3, 2018

Phasendiagramm des Multi-Orbitalen Hubbard Modells

Vorgelegt von

Bence Temesi

BACHELORARBEIT

Fakultät für Physik

Ludwig-Maximilians-Universität München

Betreuer:

Prof. Dr. Jan von Delft

München, August 3, 2018

Contents

Name: Bence Temesi
Studienrichtung: Bachelor Physik
E-Mail: Bence.Temesi@physik.uni-muenchen.de

Erklärung

Hiermit erkläre ich, die vorliegende Arbeit selbstständig verfasst zu haben und keine anderen als die in der Arbeit angegebenen Quellen und Hilfsmittel benutzt zu haben.

Bence Temesi München, August 3, 2018

Acknowledgement

I would like to thank Professor Jan von Delft for the opportunity to write my bachelor thesis at the chair of Theoretical Solid State Physics. In the last weeks I have gathered a lot of valuable knowledge and all of it will be really useful for the future. I am also very thankful to Fabian Kugler who answered every single question I could come up with and helped me understand all the basics.

1 Introduction

Applying the principles of quantum mechanics to many-body physics led to a better understanding of strongly correlated electronic systems. It still poses a challenge to describe these systems realistically, but both the theoretical and experimental sides are improving with every single day. Strong electronic correlations arise mostly in materials with partially filled d- or f-shells (such as iron, copper, vanadium and their oxides) and they are of great interest. Whether the material is in its metallic or insulating state, depends on many parameters, e.g. temperature, chemical potential, electron filling (of an atomic site), magnitudes of the interaction (intra- and inter-band interactions) and of the kinetic scales.
To describe these strongly correlated systems, a today widely accepted model was introduced, the Hubbard-model [1, 2, 3]. Accordingly, it captures the competition between the kinetic and interaction term of the electrons on an arbitrary lattice, which is a key feature of these systems. Taking the two limits, the atomic limit with a powerful Coulomb repulsion and the non-interacting limit, gives us better insight how these materials behave. For the first case, one can observe the Mott phenomenon, where the electrons become localized and hence the solid is a Mott insulator. As for the latter case, the electrons are itinerant, i.e. they move (quantum tunnel) freely between the atomic sites and hence the solid is a conductor. The ambition of our dissertation is to understand the nature of the Mott-Hubbard metal-insulator transition of a *multi-band* Hubbard model under controlled conditions and parameters. In this more complex model we will see the importance of the Hund's coupling and see how it affects the Mott transitions. Finally, we will observe the physics of the crystal fields where the orbital-degeneracy of the multi-orbital Hubbard model is lifted.
Striving for a numerical solution of the Hubbard Hamiltonian, we will treat the whole system in the Dynamical Mean-Field Theory (DMFT) [4, 5, 6]. This theory provides a non-perturbative way to handle strongly correlated systems. Basically, it assumes a local self-energy with fully screened Coulomb intearactions and it maps self-consistently the many-particle lattice onto an effective quantum impurity model. The results become exact in the limit of infinite dimenisons but during the theoretical calculations in the framework of the DMFT one stumbles upon fermionic many-particle wave functions, which are infamously difficult to handle. In order to make the numerical calculations tractable, there were many approaches considered in the last few decades [7, 8, 9]. In the following we will use the Numerical Renormalization Group (NRG) as the *impurity solver* for the DMFT [10, 11, 12]. The NRG method provides an iterative way to diagonalize the Hamiltonian of the effective impurity model and with that a way to determine its energy spectrum (or its spectral function). As we will see, it is crucial for the DMFT iterations to have NRG results with sufficient accuracy, because otherwise the computations can lead to unreliable outcomes.
The resulting characteristic spectral functions give information about the physical properties of the strongly correlated systems. By analysing them, we can tell if the system is in a metallic or in a Mott insulating phase at different interactions and we can map out the phase diagrams of the Hubbard models. In these phase diagrams we will see a coexistence regime between the pure phases, called the hysteresis, where we can stabilize both metallic and insulating solutions. Our main question is, how does the phase diagram (and the hysteresis) look like if we vary the interaction terms. Concerning this question, we will investigate the single-band, degenerate and semi-degenerate (or crystallic) multi-band Hubbard models.

2 Theory

2.1 Dynamical Mean-Field Theory (DMFT)

A wide variety of numerical techniques and analytical methods have been used to treat strongly correlated electron systems. Many physical characteristics come from the competition of the kinetic energy and Coulomb interaction of the electrons. One possible way to treat the correlated lattice fermions is to take the limit of infinite dimensions [4, 5, 6]. In this limit the computations are simplified while the competition of energies is retained. A. Georges and G. Kotliar managed to map the Hubbard model (a lattice model) onto a self-consistent quantum impurity model - a set of local quantum mechanical degrees of freedom that interacts with a non-interacting bath [5]. This construction provides the basis of the Dynamical Mean-Field Theory (DMFT) of correlated electrons. Considering the DMFT while increasing the number of neighbours (like in the limit of infinite dimensions: $d \to \infty$) leads to exact solutions. How the correlated system is affected by computing with high dimensions can be seen in Appendix A.
Thus the main principle of the mean-field theory is to map (to reduce) a many-body lattice problem to a single-site problem with effective and local parameters. Accordingly, it takes out a single atomic site while the rest of the crystal acts as a reservoir of non-interacting electrons that can be absorbed in the site. The environment allows the atom to make transitions between different configurations, i.e. to change the number of the electrons on the site. This constant change of the on-site electron filling makes the mean-field theory *dynamical*. In order to include the ability of electrons to hop on and off a given atomic site (impurity) on a time scale $1/\omega$, a hybridization term $\Delta(\omega)$ needs to be introduced. This approach is like the Anderson impurity model [13] but with an additional self-consistency condition, discussed with (2.1.26). For the computations of the quantum impurity model, a certain analytical or numerical method is required. There are different methods, such as the Quantum Monte Carlo (QMC) method [7, 8] or the Exact Diagonalization (ED) [9]. In our case, we will use the Numerical Renormalization Group (NRG), which will be discussed in Sec. 2.2. The strength of the hybridization has a significant influence on the physics of the material. If the hybridization is small, the electrons are almost entirely localized at a lattice site, on the other hand if it is large, then the electrons can move more freely throughout the crystal. As we can see, it is similar to the nature of the Hubbard model, because there is a competition between the localized and de-localized tendencies. Thus the transformation of the Hubbard model into the Single-Impurity Anderson Model (SIAM) is well-founded.

In order to derive the general DMFT equations we assume that both the band structure (which leads to a certain kinetic amplitude t) and the strength of the Coulomb interaction (V) are known. In general the Hubbard Hamiltonian can be written as

$$H = \sum_{ij\alpha\beta\sigma} t_{ij}^{\alpha\beta} c_{i\alpha\sigma}^{\dagger} c_{j\beta\sigma} + \frac{1}{2} \sum_{\substack{ijkl \\ \alpha\beta\gamma\delta\sigma\sigma'}} V_{ijkl}^{\alpha\beta\gamma\delta} c_{i\alpha\sigma}^{\dagger} c_{j\beta\sigma'}^{\dagger} c_{l\delta\sigma'} c_{k\gamma\sigma} \ . \tag{2.1.1}$$

First for our purpose, we are only interested in a single band, thus the on-site Hubbard interaction simplifies to $U = V_{iiii}$. The extension to the multi-band model affects the local interactions (which is described in the section of the multi-orbital Hubbard model (2.4.4) and also the coupling or hybridization to the non-interacting bath Appendix D.

$$H = H_{kin} + H_{int} \tag{2.1.2}$$

$$\text{with} \quad H_{int} = U \sum_i n_{i\uparrow} n_{i\downarrow} \ , \tag{2.1.3}$$

$$H_{kin} = \sum_{\langle ij \rangle \sigma} t_{ij} c_{i\sigma}^{\dagger} c_{j\sigma} = \sum_{\mathbf{k}\sigma} \varepsilon_{\mathbf{k}} c_{\mathbf{k}\sigma}^{\dagger} c_{\mathbf{k}\sigma} \ , \tag{2.1.4}$$

where t_{ij} in the tight-binding approximation is the hopping amplitude among the nearest neighbour sites i and j. The Fourier transform of t_{ij} yields the dispersion relation $\varepsilon_{\mathbf{k}}$ in momentum space. In order to describe a dynamical, strongly correlated system, an important dynamical quantity, the retarded one-particle Green's function needs to be introduced ([14] Sec. 5). In

general the Green's function G_{AB} is defined as the expectation value of operators A and B measured at different times t

$$G_{AB}(t) = \langle\langle A; B\rangle\rangle_t \equiv -i\Theta(t)\langle\{A(t), B(0)\}\rangle_T \,. \tag{2.1.5}$$

The system is considered as a grand canonical, thermodynamic ensemble, i.e. the expectation value of a physical observable O is given by

$$\langle O(\mu)\rangle_T = \frac{\mathrm{Tr}\left[Oe^{-\beta(H-\mu N)}\right]}{\mathrm{Tr}\left[e^{-\beta(H-\mu N)}\right]} \,,$$

with the chemical potential μ, particle number N and the inverse temperature $\beta \equiv \hbar/k_B T$. In imaginary time if the operators A and B are the fermionic annihilation and creation operators $c_\nu(\tau), c_\nu^\dagger(0)$, then the Green's function gives the probability amplitude for the propagation of a particle (or hole) excitation with arbitrary set of quantum numbers $\nu = \{\text{spin, momentum, orbital}\}$, that is, the probability amplitude required to create an electron with spin σ ($\uparrow$ or $\downarrow$), momentum $\mathbf{k}$, band m at a site i at imaginary time $\tau = 0$ and to destroy it at the same site (local) at a later time τ

$$G(\nu;\tau) \equiv -\langle Tc_\nu(\tau)c_\nu^\dagger(0)\rangle_T \equiv -\begin{cases} \langle c_\nu(\tau)c_\nu^\dagger(0)\rangle_T \,, & \text{if} \quad \tau > 0 \\ -\langle c_\nu^\dagger(0)c_\nu(\tau)\rangle_T \,, & \text{if} \quad \tau \leq 0 \,, \end{cases} \tag{2.1.6}$$

with T, the fermionic time ordering operator. The time evolution of the operators is provided by the Heisenberg picture, with $A(\tau) = e^{H\tau}Ae^{-H\tau}$. Using the Fourier transformation, the Green's function in momentum space with imaginary times (also called as Matsubara Green's function, more details in [15]) yields

$$G(\nu; i\omega_n) = \int_0^\beta d\tau\; G(\nu;\tau)e^{i\omega_n\tau}, \qquad G(\nu;\tau) = T\sum_{n=-\infty}^{+\infty} G(\nu; i\omega_n)e^{-i\omega_n\tau} \,, \tag{2.1.7}$$

with fermionic Matsubara frequencies $i\omega_n = 2\pi T(n+1/2)$. The Green's function of a free single-particle, using the definition and the time evolution in the Heisenberg picture (Appendix C), can be written as

$$G_0(\nu;\omega) = \frac{1}{i\omega - \varepsilon_\mathbf{k}} \,, \qquad G_0^{ret}(\nu;\omega) = \frac{1}{\omega - \varepsilon_\mathbf{k} + i0^+} \,. \tag{2.1.8}$$

$G_0^{ret}(\nu;\omega)$ is the Green's function which is defined only on the time domain that involves real-time Heisenberg operators. The subscript '0' denotes that these are the Green's functions of the free, non-interacting particles. A more practical and measurable quantity is the spectral function $A(\nu;\omega)$, defined as:

$$A(\nu;\omega) \equiv -\frac{1}{\pi}\mathrm{Im}G^{ret}(\nu;\omega) \qquad \Rightarrow \qquad A_0(\nu;\omega) = \delta(\omega - \varepsilon_\mathbf{k}) \,, \tag{2.1.9}$$

where in the second part, the Green's function of the free particle $G_0^{ret}(\nu;\omega)$ was inserted and a Dirac identity was used, described in Appendix B. (2.1.9) shows a δ-peak right at the excitation energy $\varepsilon_\mathbf{k}$. The spectral function of a many-body system is hence a composition of many δ-functions, weighted by the probabilities of each excitations. Considering the probability amplitudes of the different transitions between the eigenstates and averaging in the grand canonical ensemble (since the particle number changes with time), one gets the Lehmann representation of the spectral function $A(\nu;\omega)$

$$A(\nu;\omega) = \frac{1}{Z}\sum_{n,m}\langle n|c_\nu^\dagger|m\rangle\langle m|c_\nu|n\rangle(e^{-\beta E_m} + e^{-\beta E_n})\delta(\omega - (E_n - E_m)). \tag{2.1.10}$$

This representation uses the set of eigenstates $\{|n\rangle\}$ of the Hamiltonian $\mathcal{H} = H - \mu N$ as basis set with the eigenvalues E_n. In (2.1.10) $Z = \mathrm{Tr}e^{-\beta(H-\mu N)}$ is the grand canonical partition function.

The spectral function $A(\nu;\omega)$ is normalized and positive semi-definite ([16], p. 134.)

$$\int_{-\infty}^{\infty} d\omega\, A(\nu;\omega) = 1\,, \quad \text{with} \quad A(\nu;\omega) \geq 0\,.$$

With these properties the spectral function $A(\nu;\omega)$ can be interpreted as a probability density, i.e. $A(\nu;\omega)d\omega$ is the probability for a particle with quantum numbers ν to have an energy lying in $[\omega, \omega + d\omega]$. Hence, the spectral function is similar to the density of states at a given energy. This is evident since the occupation n_ν of a given state $|\nu\rangle$ is for fermions given by

$$\int_{-\infty}^{\infty} d\omega\, A(\nu;\omega) n_F(\omega) \overset{\substack{T\to 0 \\ n_F\to\Theta(-\omega)}}{=} \int_{-\infty}^{0} d\omega\, A(\nu;\omega) = \bar{n}_\nu \equiv \langle c_\nu^\dagger c_\nu \rangle_T\,, \tag{2.1.11}$$

with the Fermi-Dirac distribution $n_F(\omega, T)$. For a given spectral function, (2.1.11) shows that if we take the integral for energies $\omega < 0$ (electron propagating from an excited state to its ground-state or equivalently hole-excitation) we get the average number of the particles with the set of quantum numbers ν. The same applies for the number of holes for the positive energies (particle-excitations) $\omega > 0$. For instance if there are more holes on the site than particles, the weight of the left side of the spectral function will be smaller relative to the right side, since the more holes the site has, the more particle-excitations are possible. Also, if the particle-state $|\nu\rangle$ is far below the Fermi surface then $\bar{n}_\nu \approx 1$, since it is unlikely that this low-energy particle gets excited. This result in fact can be derived from (2.1.11), since $\epsilon_\nu \ll E_F$ and the width of $A(\nu;\omega)$ is also small compared to E_F makes the Fermi function $n_F(\omega, T)$ approximately unity. The rest, $A(\nu;\omega)$, integrates to 1, hence the expected result follows. Using the spectral function one can express the Green's function in the spectral representation, which is basically a sum over the δ-peaks of the electrons energies (Appendix B)

$$G_0^{ret}(\nu;\omega) = \int_{-\infty}^{\infty} d\omega' \, \frac{A(\nu;\omega')}{\omega - \omega' + i0^+}\,. \tag{2.1.12}$$

When electron-electron interactions are present the spectral function changes from the ideal δ function to a more broadened peak. Due to these interactions, the electrons cause changes in their environment which result in energy-shifts and hence the particles' energy (effective mass) has to be corrected by the *electron self-energy*: $\Sigma_\sigma(\mathbf{k}, \omega)$. It is related to the free and dressed Green's functions (or propagators) G_0 and G. The latter one considers the higher-order perturbation terms, an inseparable cloud of electron-positron pairs and photons around the propagating electron. The relation is given by

$$G = G_0 + G_0 \Sigma G \quad \Rightarrow \quad \Sigma = G_0^{-1} - G^{-1}\,. \tag{2.1.13}$$

(2.1.13) is also known as the Dyson equation which can be expressed with Feynman diagrams. Σ_σ is the sum of all irreducible diagrams without the first term (shown as a simple line), which represents the free particle. The second term in the sum is the first correction in the Born approximation.

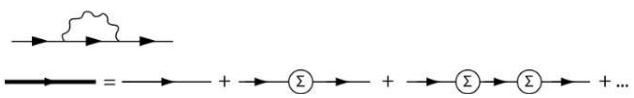

The irreducible self-energy is a dynamical term which changes together with the potential as the electron fields move in the medium. However it becomes a purely local quantity as the dimension of the correlated lattice approaches infinity (Appendix A), which makes it significantly easier to calculate

$$\Sigma_\sigma(\mathbf{k}, \omega) \overset{d\to\infty}{=} \Sigma_\sigma(\omega)\,. \tag{2.1.14}$$

The self-energy $\Sigma_\sigma(\omega)$ is not just momentum-independent in $\mathbf{k}$ space, but also is a functional only of the local Green's function $G_\sigma(\omega)$, because all the interactions of an electron with the environment happens on the electron's site. The self-energy has a direct impact on the Green's

function (2.1.8),

$$G_{\mathbf{k}\sigma}(\omega) = \frac{1}{\omega + \mu - \varepsilon_{\mathbf{k}} - \Sigma_\sigma(\omega)} = G^0_{\mathbf{k}\sigma}(\omega - \Sigma_\sigma(\omega)) \,, \tag{2.1.15}$$

and in particular, the local Green's function becomes

$$\begin{aligned} G_\sigma(\omega) &= \int \frac{d^d k}{(2\pi)^d} \frac{1}{\omega + \mu - \varepsilon_{\mathbf{k}} - \Sigma_\sigma(\omega)} \\ &= \int_{-\infty}^{\infty} d\varepsilon \, \frac{\rho_0(\varepsilon)}{\omega + \mu - \varepsilon - \Sigma_\sigma(\omega)} \,. \end{aligned} \tag{2.1.16}$$

This last equation provides a relation between the local self-energy, the local Green's function and the free density of states $\rho(\varepsilon) = 1/(2\pi)^d \int d^d k \; \delta(\varepsilon - \varepsilon_{\mathbf{k}})$. The Green's function depends only on the dispersion ε via the free density of states $\rho(\varepsilon)$.

The Green's function and the self-energy in (2.1.15) can be now redefined as the lattice Green's function and self-energy: $G_{latt}(\omega)$ and $\Sigma_{latt}(\omega)$. In order to map the lattice model onto an impurity model with effective parameters, one needs to calculate the impurity Green's function Σ_{imp}. Since interactions only enter locally via the momentum-independent self-energy in DMFT, the impurity self-energy will equal to the lattice self-energy (considering equal local interactions):

$$\Sigma_{latt}(\omega) = \Sigma_{imp}(\omega) \equiv \Sigma(\omega) \,. \tag{2.1.17}$$

As a consequence, the dynamics of the lattice model, which is contained in its local lattice Green's function, can be determined via the Green's function of the impurity model. Hence, the mapping has to fulfil the condition

$$G_{latt}(\omega) \stackrel{!}{=} G_{imp}(\omega) \,. \tag{2.1.18}$$

For the single-band Hubbard Hamiltonian, the effective quantum impurity model is the single impurity Anderson model (SIAM)

$$H_{SIAM} = H_{imp} + H_{bath} + H_{hyb} \,, \tag{2.1.19}$$

$$H_{imp} = \sum_\sigma \varepsilon_d d^\dagger_\sigma d_\sigma + U d^\dagger_\uparrow d_\uparrow d^\dagger_\downarrow d_\downarrow \,, \tag{2.1.20}$$

$$H_{bath} = \sum_{k \in 1.BZ} \sum_\sigma \varepsilon_k c^\dagger_{k\sigma} c_{k\sigma} \,, \tag{2.1.21}$$

$$H_{hyb} = \sum_{k \in 1.BZ} \sum_\sigma V_k (d^\dagger_\sigma c_{k\sigma} + c^\dagger_{k\sigma} d_\sigma) \,, \tag{2.1.22}$$

where $d^{(\dagger)}_\sigma$ denotes the annihilation (creation) operator for an electron of spin $\sigma = \uparrow, \downarrow$ on the impurity and $c^{(\dagger)}_\sigma$ in the bath respectively. ϵ_d is the local energy level of the impurity site and has to be equal to the local single-particle level $-\mu$ of the lattice. The local site has four different states in the one-band lattice model: $|0\rangle, |\uparrow\rangle, |\downarrow\rangle$ and $|\uparrow\downarrow\rangle$. In the last case, the electrons have a repulsive force U on each other. This interaction in the SIAM is equal to the local interaction of the Hubbard model. The rest of the lattice is described by an effective bath of non-interacting electrons (H_{bath}), which couples to the impurity (H_{hyb}) via the hopping amplitude given by V_k. Thus, the local impurity model allows charge and spin fluctuations on the site, which can lead to transitions between different quantum phases. The effect of the external bath onto the impurity is fully contained in the hybridization function (Appendix D),

$$\Delta(\omega) = \sum_k \frac{V_k^2}{\omega - \varepsilon_k} \,. \tag{2.1.23}$$

The local interacting Green's function of the effective impurity model is completely given in terms of the hybridization function $\Delta(\omega)$ and the self-energy $\Sigma(\omega)$:

$$G_{imp}(\omega) \equiv \langle\langle d; d^\dagger \rangle\rangle_\omega = \frac{1}{\omega - \varepsilon_d - \Delta(\omega) - \Sigma(\omega)} \,, \quad \varepsilon_d = -\mu \,. \tag{2.1.24}$$

This can be derived from the equation of motion (Appendix B),

$$\omega\langle\langle d; d^\dagger\rangle\rangle_\omega = \langle\{d, d^\dagger\}\rangle_T - \langle\langle[H, d]; d^\dagger\rangle\rangle_\omega \,. \tag{2.1.25}$$

In order to map the original lattice onto the effective impurity model, one needs to calculate the local lattice Green's function with the impurity Green's function, using: $G_{latt}(\omega) \stackrel{!}{=} G_{imp}(\omega)$. Inserting $G_{imp}(\omega)$ from (2.1.24) yields the self-consistency condition for the Green's function

$$G_{latt}(\omega)^{-1} + \Sigma(\omega) = \omega - \varepsilon_d - \Delta(\omega) = G^0_{imp}(\omega)^{-1} \,, \tag{2.1.26}$$

which also leads to a self-consistency condition for the imaginary part of the hybridization,

$$\begin{aligned} \Gamma(\omega) &= -\operatorname{Im}\Delta(\omega) = -\pi \sum_k V_k^2 \delta(\omega - \varepsilon_k) \\ &= \operatorname{Im}(G_{latt}(\omega)^{-1} + \Sigma(\omega)) \,, \end{aligned} \tag{2.1.27}$$

where $\Gamma(\omega)$ is also called the Weiss effective field. These DMFT equations can be solved iteratively (Fig. 1) leading to a solution for the hybridization function $\Gamma(\omega)$, the local self-energy $\Sigma(\omega)$, the local Green's function and accordingly the spectral function $A(\omega)$.

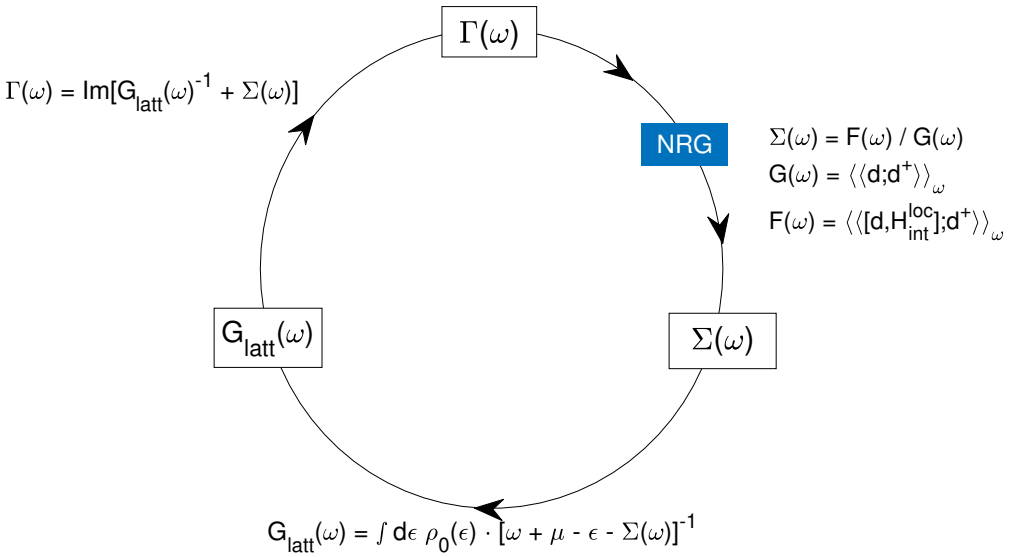

Figure 1: Schematic DMFT iteration loop, (i) starting with the input hybridization $\Gamma(\omega)$, (ii) then the numerical calculation with NRG to determine the local self-energy $\Sigma(\omega)$, (iii) computing the lattice Green's function $G_{latt}(\omega)$ and (iv) using the self-consistency condition to find the new hybridization function $\Gamma'(\omega)$ which serves as the input for the next iteration.

In order to begin with the iteration process, one needs an arbitrary starting hybridization function $\Gamma_0(\omega)$. Using Numerical Renormalization Group (NRG) as the *impurity solver* returns the self-energy $\Sigma(\omega)$ of the SIAM. This has to be equal to the lattice self-energy (2.1.17) and thus can be inserted into the integral expression (2.1.16) with a given density of states to compute the lattice Green's function. Finally with the self-consistency condition (2.1.27) a new hybridization function is determined and the first DMFT iteration loop closes. This newly found $\Gamma(\omega)$ serves as the input for the next loop, and the iterative procedure goes on until it converges to a stable and most of the time unique solution. The solution is independent of the initial hybridization, although with the right input the convergence can be reached faster. Finally, using the definition in (2.1.9) one has the spectral function, which shows the dynamics of the strongly correlated many-body system more clearly.

With the intention of making the DMFT calculations simpler, a special type of lattice, the Bethe lattice will be used in the limit of infinite dimensions [17]. In d dimensions the Bethe lattice is a graph where each lattice site has d nearest neighbours without containing cycles. The only place where the type of the lattice affects the DMFT computations is in (2.1.16) where for the Bethe lattice the non-interacting DOS has a semi-elliptic form

$$\rho_0^B(\varepsilon) = \frac{2}{\pi D}\sqrt{1-\left(\frac{\varepsilon}{D}\right)^2}\,, \tag{2.1.28}$$

with $\varepsilon \in [-D, D]$ and with the half bandwidth $D = W/2$. The local lattice Green's function is the Hilbert transform of the non-interacting density of states, which with the Bethe lattice yields

$$G_{latt}(\xi) = \int_{-\infty}^{\infty} d\varepsilon\, \frac{\rho_0(\varepsilon)}{\xi-\varepsilon} \quad \overset{\rho_0 := \rho_0^B}{\Longrightarrow} \quad G_{latt}(\xi) = \frac{2}{D^2}\left(\xi - \sqrt{\xi^2 - D^2}\right)\,, \tag{2.1.29}$$

with $\xi = \omega + \mu - \Sigma(\omega)$ and $\operatorname{Im}\xi = -\operatorname{Im}\Sigma(\omega) > 0$ (for the retarded Green's function). In the second step the continued fraction expansion was used ([18], Appendix D). By inserting (2.1.29) in (2.1.26) one can derive the following relation

$$\omega - \varepsilon_d - \Delta(\omega) = \omega + \mu - \left(\frac{D}{2}\right)^2 G_{latt}\,. \tag{2.1.30}$$

Furthermore, it directly leads to the expressions

$$\Delta(\omega) = \left(\frac{D}{2}\right)^2 G_{latt}(\omega) \quad \text{and} \quad \frac{\Gamma(\omega)}{\pi} = \left(\frac{D}{2}\right)^2 A(\omega)\,. \tag{2.1.31}$$

In the second part, the definition of the spectral function was used, $A(\omega) = -\frac{1}{\pi}\operatorname{Im} G_{latt}(\omega)$. (2.1.31) shows that for the Bethe lattice the hybridization function $\Gamma(\omega)$ and the spectral function $A(\omega)$ have the same form (up to a constant factor).
The most time-consuming part of the DMFT procedure is the numerical computation of the self-energy from a certain hybridization function. The accuracy of the impurity solver (NRG) determines the overall success of the DMFT. In the next chapter we will discuss the methodology of the NRG in the DMFT framework.

2.2 Numerical Renormalization Group (NRG)

To investigate lattice models in the DMFT we need an *impurity solver*, the Numerical Renormalization Group (NRG) to compute the full frequency dependence of the self-energy. The Hubbard model is mapped onto a single-impurity model (SIAM) defined by arbitrary input parameters (e.g. $U, T, \mu, \Delta(\omega)$). NRG was developed by K.G. Wilson to solve the Kondo model in a fully non-perturbative way [10, 11] and has been discussed in the DMFT framework more thoroughly in [12]. It has been later shown that the NRG allows for a very accurate computation of dynamical properties of various impurity models, such as the SIAM [19, 20]. It has already been used to investigate the Mott transition [20, 21, 22].

In general a quantum impurity model consists of a discrete quantum system with a small number of degrees of freedom that is embedded in a macroscopic bath of non-interacting fermions. Each system can be in principle solved exactly on its own, however, the coupling (hybridization) leads to strongly correlated, complicated quantum many-body phenomena. Let us take the Hamiltonian from (2.1.19),

$$H = H_{imp} + H_{bath} + H_{hyb}\,, \tag{2.2.1}$$

where the impurity Hamiltonian H_{imp} may not only contain the Coulomb repulsion but also the Hund's coupling terms for a multi-band Hubbard model. Since by assumption the impurity has a small amount of degrees of freedom, it can be diagonalised exactly. As for the bath term H_{bath}, it describes a continuous excitation spectrum covering a broad range of energies. Since there is no interactions between the bath fermions, the many-body states are just a product state of the

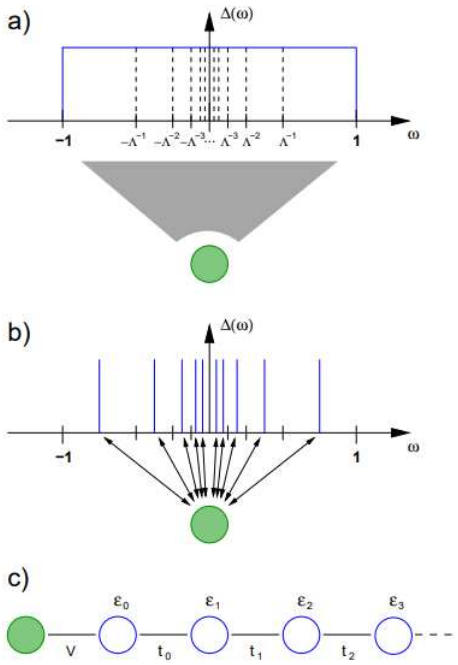

Figure 2: Schematic figure of the NRG steps for the SIAM (taken from [12]). In (a) a logarithmic discretization (with the characteristic parameter Λ is used to make a finite set of energy intervals from the continuous bath spectrum; (b) approximates each intervals with a single state; (c) transforms the resulting discretized model into the semi-infinite Wilson Hamiltonian chain, where the impurity couples to the first conduction electron via the hybridization V.

single-particle states and therefore H_{bath} is in principle also diagonalizable.
Before going into more technical details, let us overview the general idea of the NRG. Since the bath can add an infinite amount of degrees of freedom to the system, the diagonalization becomes a numerical problem. In order to overcome this problem, one needs to discretize the bath to finite amount of degrees of freedom. The constant bath spectral function is considered within the interval $\omega \in [-D, D]$ (with the half bandwidth $D := 1$, note that later in our computations $D = 2$), where the chemical potential μ which is also the Fermi energy E_F for $T = 0$, is set to zero. (Note, that μ can be set zero, because it is just a shift in the energy spectrum.) First, a division of the energy support of the bath spectral function is needed to create a set of logarithmic intervals, see Fig. 2 (a) (both figures used in this NRG section is adapted from [12]). The NRG discretization parameter Λ defines a set of discretization points, $\pm\Lambda^{-n}$, with $\Lambda > 1$ and $n = 0, 1, 2, ...$ The resolution is improved as $\Lambda \to 1$ and for $\Lambda = 1$ it returns the continuum limit. This partition is followed by the discretization, i.e. a reduction of the continuous spectrum to a discrete set of states. Every interval closed in by a pair of logarithmic points, is approximated by a single state, see Fig. 2 (b). The logarithmic nature of the discretization is crucial, because this allows to resolve even the lowest relevant energy scales of the system and because it provides a separation of the energy scales and therefore allows to iteratively diagonalize the low-energy part. We are interested in the energies near the Fermi energy (or the chemical potential for $T \to 0$), thus the Mott-Hubbard metal-insulator transition can be investigated with fewer states which contain more essential information of the physical behaviour of the system. The resulting discretized model is mapped onto a semi-infinite tight-binding chain with the impurity (filled circle) corresponding to the first site of this chain. The final step is the iterative diagonalization of the Hamiltonian chain, shown in Fig. 2 (c). The Hilbert space is exponentially growing as the chain is becoming longer, which makes the numerical diagonalization more and more time-consuming and impossible. This is resolved by the scaling of the coupling, i.e. the hopping matrix elements between the sites decay exponentially with the distance from the impurity, $t_n \propto \Lambda^{-n/2}$. Adding a site to the chain corresponds to decreasing the relevant energy scale by a factor $\sqrt{\Lambda}$. Since t_n fall off exponentially for the newly added sites, the energy they contribute with becomes drastically smaller. That is, a so called truncation can be applied, where after each step only

the energetically lowest lying N_s many-particle states are retained and used to build up the Hamiltonian matrices of the next iteration step, hence keeping the size of the Hilbert space fixed as one proceeds along the Wilson chain.

As in the previous, DMFT section (Sec. 2.1), it was shown that the effective quantum impurity model of the Hubbard Hamiltonian can be interpreted with the SIAM. Consequently, H_{SIAM} will be used here for the NRG calculations as well. The imaginary part of the hybridization function is $\Gamma(\omega) = \pi \sum_{k\in 1.BZ} V_k^2 \delta(\omega - \varepsilon_k)$. A possible one-dimensional energy representation of H_{SIAM} [23] is achieved by replacing the discrete bath operators $c_{k\sigma}^{(\dagger)}$ by the continuum bath operators $a_{\varepsilon\omega}^{(\dagger)}$, using the transformation:

$$c_{k\sigma}^{(\dagger)} \quad \rightarrow \quad \frac{a_{\varepsilon\sigma}^{(\dagger)}}{\sqrt{\rho_0(\varepsilon)}}, \quad \text{and} \quad \sum_{k\in 1.BZ} \rightarrow \int_{-1}^{1} d\varepsilon\, \rho_0(\varepsilon)\,. \tag{2.2.2}$$

$\rho_0(\varepsilon)$ is the non-interacting density of states (in our case of the Bethe lattice, $\rho_0^B(\varepsilon)$). The transformation is defined such that, $\{a_{\varepsilon\sigma}, a^\dagger_{\varepsilon'\sigma'}\} = \delta(\varepsilon - \varepsilon')\delta_{\sigma\sigma'}$. Applying this transformation to the SIAM Hamiltonian H_{SIAM}:

$$H = H_{imp} + \sum_\sigma \int_{-1}^{1} d\varepsilon\, \varepsilon\, a^\dagger_{\varepsilon\sigma} a_{\varepsilon\sigma} + \sum_\sigma \int_{-1}^{1} d\varepsilon \sqrt{\frac{\Gamma(\varepsilon)}{\pi}} (d^\dagger_\sigma a_{\varepsilon\sigma} + h.c.)\,, \tag{2.2.3}$$

where the hybridization function has now the form:

$$\Gamma(\varepsilon) \equiv \pi \rho_0(\varepsilon) V^2(\varepsilon)\,. \tag{2.2.4}$$

The resulting Hamiltonian is then submitted to the logarithmic discretization. Using the discretization parameter $\Lambda > 1$ on the energy scale leads to the discretization points:

$$x_n = \pm \Lambda^{-n} \quad \text{with} \quad n = 0, 1, 2, \ldots\,, \tag{2.2.5}$$

where the length of the intervals decrease logarithmically $d_n \equiv x_n - x_{n+1} = \Lambda^{-(n+1)}(\Lambda - 1)$, for $x_n > x_{n+1}$. Typical values for Λ are between 1.5 and 4, for $\Lambda \rightarrow 1$, the continuum limit is recovered. To each of these intervals there is a mean energy ξ_n ordered,

$$\xi_n^\pm = \frac{\int^{\pm,n} d\varepsilon\, \Gamma(\varepsilon)\varepsilon}{\int^{\pm,n} d\varepsilon\, \Gamma(\varepsilon)} =: \frac{1}{(\gamma_n^\pm)^2} \int^{\pm,n} d\varepsilon\, \Gamma(\varepsilon)\varepsilon. \tag{2.2.6}$$

Here we have defined

$$\int^{+,n} d\varepsilon \equiv \int_{x_{n+1}}^{x_n} d\varepsilon \quad , \quad \int^{-,n} d\varepsilon \equiv \int_{-x_n}^{-x_{n+1}} d\varepsilon\,.$$

Finally, one arrives at the discretized Hamiltonian (proper derivation in [12]), where the bath Hamiltonian is approximated by a single state per interval,

$$H = H_{imp} + \sum_{n\sigma} \xi_n a^\dagger_{n\sigma} a_{n\sigma} + \sum_\sigma (d^\dagger_\sigma \sum_n \gamma_n a_{n\sigma} + \text{h.c.})\,, \tag{2.2.7}$$

with the proper fermionic operators which annihilate (create) an electron with spin σ in each bath interval respectively,

$$a_{n\sigma}^{(\dagger)} \equiv \frac{1}{\gamma_n} \int^{\pm,n} d\varepsilon \sqrt{\frac{\Gamma(\varepsilon)}{\pi}} a_{\varepsilon\sigma}^{(\dagger)}\,.$$

A commonly used technique to improve the accuracy of the NRG calculations for physical quantities is to average over various discretizations for a fixed Λ. This procedure is also called z-averaging (or z-shifting along the energy axis), where the discretization points are modified to:

$$x_n = \begin{cases} 1 & : n = 0 \\ \Lambda^{-(n+z)} & : n \geq 1 \end{cases} \tag{2.2.8}$$

This averaging is essential to enhance the resolution, because in the Wilson chain the bath character is degraded due to the reduction of the fermionic levels.
Following the thought process of [24], the next step of the NRG procedure is to transform the discretized Hamiltonian (2.2.7) into a semi-infinite chain form, where the first site represents the impurity $d_\sigma^{(\dagger)}$ with its degrees of freedom and it couples to a single fermionic degree of freedom from the conduction band $f_\sigma^{(\dagger)}$, with coupling (hybridization) $\sqrt{\xi_0}$. New conduction band states $f_\sigma^{(\dagger)}$ are present which are not equivalent to the non-coupled bath states,

$$f_{n\sigma}^{(\dagger)} = \frac{1}{\sqrt{\xi_0}} \sum_n \gamma_n a_{n\sigma}^{(\dagger)} \,, \tag{2.2.9}$$

with the normalization constant

$$\xi_0 = \sum_n \gamma_n^2 = \int_{-1}^{1} d\varepsilon \, \frac{\Gamma(\varepsilon)}{\pi} \,. \tag{2.2.10}$$

The transformation is achieved via a tridiagonalization procedure using the Lánczos algorithm [25] which leads to the following Hamiltonian

$$H = H_{imp} + \sqrt{\xi_0} \sum_\sigma (d_\sigma^\dagger f_{0\sigma} + \text{h.c.}) + \sum_{\sigma,n=0}^{\infty} \left[\epsilon_n f_{n\sigma}^\dagger f_{n\sigma} + t_n (f_{n\sigma}^\dagger f_{n+1\sigma} + \text{h.c.}) \right] . \tag{2.2.11}$$

The remaining sites of the bath couple to their next neighbour via the decreasing hopping matrix element $t_n \propto \Lambda^{-n/2}$ and each new electron on these sites contribute to the Hamiltonian with energy ϵ_n. For the single-band case, the possible eigenstates of a site are $|\sigma_n\rangle = \{|0\rangle, |\uparrow\rangle, |\downarrow\rangle, |\uparrow\downarrow\rangle\}$. Hence by adding a new site to the Wilson chain, the Hilbert space grows exponentially, as 4^n. We can also consider a more complex SIAM, where every site has 3 bands, i.e. the number of eigenstates is $4^3 = 64$ for just one site and 64^n for n sites. This complexity makes it impossible to keep all the states in the calculation. Due to the rapid decrease of the hopping matrix t_n, Wilson created a truncation procedure in which only the states with the lowest energies are kept. Thus, the size of the Hilbert space is fixed by adding a new site to the chain and the high-energy states do not change the very low frequency behaviour and can be neglected.

In order to calculate the eigenenergies of the chain, an iterative renormalization group (RG) procedure needs to be introduced. This was first done by K.G. Wilson in his work [10]. The Wilson chain describes a series of Hamiltonians H_N ($N = 0, 1, 2, ...$) which approaches H (2.2.11) in the limit $N \to \infty$.

$$H = \lim_{N\to\infty} \Lambda^{-N/2} H_N \,, \tag{2.2.12}$$

with

$$H_N = \Lambda^{N/2} \left[H_{imp} + \sqrt{\xi_0} \sum_\sigma (d_\sigma^\dagger f_{0\sigma} + \text{h.c.}) + \sum_{\sigma,n=0}^{N} \epsilon_n f_{n\sigma}^\dagger f_{n\sigma} + \sum_{\sigma,n=0}^{N-1} t_n (f_{n\sigma}^\dagger f_{n+1\sigma} + \text{h.c.}) \right] . \tag{2.2.13}$$

For convenience the factor $\Lambda^{N/2}$ is applied to cancel the N-dependence of t_{N-1}, which is the hopping amplitude between the last two sites of H_N. From (2.2.13) one can create a recursion relation for H_{N+1} as the following,

$$H_{N+1} = \sqrt{\Lambda} H_N + \Lambda^{N/2} \sum_\sigma \varepsilon_{N+1} f_{N+1\sigma}^\dagger f_{N+1\sigma} + \Lambda^{N/2} \sum_\sigma t_N (f_\sigma^\dagger f_{N+1\sigma} + \text{h.c.}) \,, \tag{2.2.14}$$

with the starting point of the sequence of the chain Hamiltonian

$$H_0 = \Lambda^{-1/2} \left[H_{imp} + \sum_\sigma \varepsilon_0 f_{0\sigma}^\dagger f_{0\sigma} + \sqrt{\xi_0} \sum_\sigma (d_\sigma^\dagger f_{0\sigma} + \text{h.c.}) \right] . \tag{2.2.15}$$

The recursion relation described by (2.2.14) and (2.2.15) acts as a renormalization group trans-

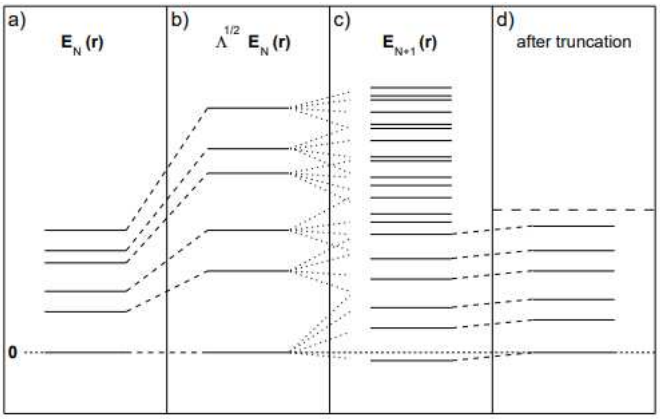

Figure 3: Truncation procedure of the NRG computations (figure taken from [12]). (a) Starting off with a set of eigenenergies $E_N(r)$, which correspond to the eigenstates $|r\rangle_N$ of the Hamiltonian H_N; (b) rescaling the energy spectrum by $\sqrt{\Lambda} > 1$; (c) adding a new conduction electron to the Wilson chain leads to much larger Hilbert space with eigenenergies E_{N+1}; (d) finally after the truncation only the lowest-lying states are retained for the next iteration.

formation R:

$$H_{N+1} = R(H_N)\,. \tag{2.2.16}$$

This has also been discussed in [24]. In general, a RG transformation takes a Hamiltonian with certain set of parameters $\vec{K}$ and maps it into another Hamiltonian of the same form, $H(\vec{K}')$, with a new set of *renormalized* parameters $(\vec{K}')$. Such a representation where the new Hamiltonian $H(\vec{K}')$ has the same form as the starting one, does not exist. But we can characterize the Hamiltonians by their eigenenergies which specify a *RG flow*. Analysing the flow of the many-particle energies $E_N(r)$ along the axis of the number of iterations N, contains information about the physics of a given model. Thus, one needs to determine the eigenenergies of the system, i.e. one has to solve the chain Hamiltonian in (2.2.12) by iterative diagonalization. The first step is to diagonalize the starting Hamiltonian H_N to obtain the eigenstates $|r\rangle_N$ and corresponding eigenenergies $E_N(r)$, with $H_N\,|r\rangle_N = E_N\,|r\rangle_N$. Inserting this diagonalized H_N into (2.2.14), leads to a new, yet to be diagonalized Hamiltonian H_{N+1}. The first term in the recursion equation (2.2.14) rescales the energies of H_N by $\sqrt{\Lambda}$, i.e. it rescales the energy spectrum since $\sqrt{\Lambda} > 1$, as shown in Fig. 3 (b). The second and third terms in the recursion are responsible for adding the new site to the chain Hamiltonian. If we consider the one-band SIAM with 4 eigenstates, then a new site increases the degeneracy of each energy level $E_N(r)$ by 4 (at the most, otherwise using the symmetries of the treated Hamiltonian can reduce this dimension growth), see Fig. 3 (c). For the diagonalization of the new Hamiltonian H_{N+1}, one needs to construct the corresponding basis as the product of the starting impurity site basis $\{|r\rangle_N\}$ and the basis of the first site of the bath $\{|s\rangle_{N+1}\}$,

$$|r,s\rangle_{N+1} = |r\rangle_N \otimes |s\rangle_{N+1}\,. \tag{2.2.17}$$

Using this basis let us construct the Hamiltonian H_{N+1} iteratively,

$$H_{N+1}(rs,r's') = {}_{N+1}\langle r,s|H_{N+1}\,|r',s'\rangle_{N+1}\,, \tag{2.2.18}$$

where the eigenstates $|\upsilon\rangle_{N+1}$ and eigenenergies $E_{N+1}(\upsilon)$ of H_{N+1} can be constructed through the unitary transformation U:

$$|\upsilon\rangle_{N+1} = \sum_{rs} U(\upsilon,rs)\,|r,s\rangle_{N+1}\,. \tag{2.2.19}$$

Fig. 3 (c) shows that, as a new degree of freedom is added to the Wilson chain, the ground-state energy becomes negative. In the following step this is set to zero for convenience. As it was discussed earlier, a truncation procedure has to be applied after a few iterations steps, since the size of the Hilbert space grows exponentially for each connected site. The reason that the

physical system still reflects its real behaviour even with this truncation scheme (which cuts off the majority of the Hilbert space) is that the high-energy states do not influence strongly the low-energy spectrum. This statement can be also proven numerically as we change the number of states which are taken into account for the following iteration step. Discarding the higher-energy states do not spoil the physical processes described by the low-energy spectrum. Such a separation of the energy spectrum can be interpreted as a perturbation of relative strength $\Lambda^{-1/2}$. For more reliable results of the self-energy, one needs to take more states into consideration, that is to increase N_s.

As already mentioned, the recursion relation (2.2.14) defines a RG transformation and with that a corresponding RG flow of the many-particle energies for adding more and more sites to the Wilson chain. With the flow diagram one can determine the various fixed points which correspond to different physical behaviours of the model. Taking the SIAM, there can be three different fixed points distinguished from each other. By computing the fix point Hamiltonians and comparing their spectrum to the numerical data, one can determine the physical meaning of the low ($N < 10$), intermediate and high ($N > 60$) lying fixed points, referring to Krishna-murthy's papers [26, 27]. In his work he explains how to determine the nature of the RG mapping of the operators by identifying the deviations from these fixed points with an appropriate perturbation of the fixed point Hamiltonians. The first two fixed points are respectively the free orbital ($V = 0$) and the local-moment fix points where a free spin decouples from the conducting band. These fix points are unstable and by adding more sites to the chain Hamiltonian, the system approaches the stable strong-coupling (hybridization) fixed point of a screened spin ($V \to \infty$). This stable fixed point is also called the Fermi-liquid fixed point, which is reached for the metallic state in the one-band Hubbard model. However, using an interleaved NRG the flow diagram is divided into several parts and it is more difficult to handle [28]. Thus in our analysis we will exploit the informations received from the spectral functions.

2.3 NRG in the Framework of DMFT

So far we have discussed the main principles of the DMFT and NRG. The purpose of this chapter is to see how the NRG is applied as a quantum impurity solver within the DMFT. As mentioned in the previous chapters, in a DMFT iteration loop the NRG is used to calculate the single-particle self-energy $\Sigma(\omega)$ from an input hybridization function $\Gamma(\omega)$.

Here the problem emerges, that using a non-constant input hybridization in DMFT, the conventional logarithmic discretization does not necessarily lead to an exponential decay of the hopping matrix elements in the Wilson chain. Without this proper decay rate which is necessary for the truncation procedure to fix the Hilbert space and to make the numerical calculations tractable, the NRG calculations lead to artefacts. To overcome this problem, there is an adaptive discretization method, introduced by R. Zitko [29, 30], which will take the shape of the hybridization function into account. In general the asymptotic nature of the discretization grid as we approach the Fermi energy, can be written as

$$\frac{d\,x(y)}{d\,y} = -\Lambda^{-y} \ln \Lambda\, C(x,y)\,, \tag{2.3.1}$$

with the continuous variable $y \equiv n + z$ and $y \in [-\infty, \infty)$, i.e. already considering an infinite amount of different z-shifts. (In our context, most of the time instead of increasing the number of z-averaging (usually stays at 2-4) for a higher accuracy, it is more efficient to raise the number of kept states or to use a finer logarithmic scaling by lowering Λ). $C(x, y)$ is an arbitrary strictly positive function with a non-zero limit for $y \to \infty$ and $x \to 0$. This last requirement assures that it has an asymptotic behaviour at $\omega = 0$. The conventional logarithmic discretization used in NRG calculations uses $C(x, y) := 1$, which leads to (2.2.8). Using the fixed discretization mesh in NRG calculations, systematic errors can occur, which cannot be corrected by increasing the number of z-shifts. These errors become prominent when the density of states vary strongly and when they are very low over considerable energy intervals, i.e. it is not satisfactory that to every interval there is a representative state ordered, even when the density of states in that partition is really low.

Zitko's adaptive discretization mesh tries to overcome this problem by lowering the density of the grid $x(y)$ in those regions where the density of states is low. This is achieved by setting $C(x, y)$ to

$$C(x, y) = \frac{f(y)}{\rho(x)} \tag{2.3.2}$$

This way, in the limit $\rho(x) \to 0$, the corresponding energy intervals will appear weakly or not at all in the discretization grid. $f(y)$ was originally set to a constant value $A = \int_0^1 \rho(\omega)d\omega$. This can also be improved by finding such a function $C(x, y)$ that weighs the regions of denser energy more.

Let us turn now to the self-energy calculations with NRG in the frame of DMFT. In order to calculate the single-particle self-energy of the SIAM, one could use the Dyson equation (2.1.13). This way we would get a numerically determined value for $G(\omega)^{-1}$ while having an exact solution for $G_0(\omega)^{-1}$, since $\Gamma(\omega)$ is given for each iteration. The sum of these Green's functions however can lead to numerical errors and thus inconsistencies. Therefore R. Bulla [21] has constructed the interaction contribution to the self-energy as the ratio of two correlation functions which was proven to give more reliable solutions,

$$\Sigma(\omega) = U\frac{F(\omega)}{G(\omega)}\,, \tag{2.3.3}$$

with the on-site correlation function $G(\omega)\,(\equiv G_{imp}(\omega))$ and the two-particle retarded Green's function $F(\omega)$

$$G(\omega) = \langle\langle d_\sigma; d_\sigma^\dagger\rangle\rangle_\omega \qquad \text{and} \qquad F(\omega) = \langle\langle d_\sigma d_{\bar\sigma}^\dagger d_{\bar\sigma}; d_\sigma^\dagger\rangle\rangle_\omega\,. \tag{2.3.4}$$

(2.3.3) holds for both $T = 0$ and $T > 0$, more details on the derivation and on the more general form for a multi-band Anderson model are given in Appendix D. Both correlation functions, $G(\omega)$ and $F(\omega)$, are calculated numerically, but they are divided by each other, i.e. only the relative error will be propagated, which leads to a numerically more stable procedure. Finally, by applying NRG to the DMFT, one gets a reliable, numerically stable solution for the self-energy of the SIAM. Inserting this resulting self-energy into (2.1.16) returns the new on-site lattice Green's function $G_{latt}(\omega)$, which also has to fulfil the self-consistency condition (2.1.26), providing the input hybridization function $\Gamma(\omega)$ for the next loop.

2.4 Hubbard Model

2.4.1 Single-Orbital Hubbard Model

The one-band Hubbard model, first introduced by J. Hubbard [1, 2, 3], has become a keystone of understanding the interactions in a system of strongly correlated electrons on a quantum mechanical level. It gives insight into the insulating, magnetic and even superconducting effects in a solid. Although it is a fairly simplified model it can still describe a solid state system realistically and gives quite accurate predictions under certain conditions. In this section, first we discuss the single-orbital Hubbard model and then the generalization of it for three fully degenerate orbitals and finally for the two-fold degenerate and one separate orbital, where the latter case is achieved via the *crystal field splitting*.
A solid consists of ions and electrons in a three-dimensional crystalline structure. Since the ions are much heavier than the electrons, we can assume a static lattice, i.e. the dynamics of the lattice sites are neglected. This means that the Hubbard Hamiltonian (HH) only consists of terms which describe the fermions' dynamics and interactions among them. In the single-orbital Hubbard model the atoms in a solid are assumed as a collection of (static) sites, each with a single orbital. The number of fermions on a site is constrained by the Pauli principle, i.e. the sites (with one orbital) can either be empty, filled with a single spin-up, a single spin-down or be doubly occupied by a pair of spin-up and -down electrons. For the last case, with 2 electrons on the same site, a Coulomb interaction appears. This interaction is screened by the strongly correlated electrons and could be approximated as purely local, which also means that the effective potential can be written as a sum of atom centred potentials. Consequently in the Hubbard model, interactions between electrons of different sites are neglected since these two-site interactions are considerably weaker. It assumes a low mobility of the band electrons, so

that the electronic band structure can be described by the superposition of the wave functions of the isolated atomic sites. In the tight-binding approximation, due to the assumed on-site interaction, the Hamiltonian matrix elements between two orbitals on different sites are given by two-centred 'hopping integrals' [31]. Thus the kinetic properties of the electrons can be understood via quantum tunnellings between the neighbouring sites. As (2.4.1) shows, hopping to another site in the second quantization is realized by destroying an electron on one site and creating it with the same spin on a neighbouring one.

$$\begin{aligned}\hat{H} &= \hat{H}_{kin} + \hat{H}_{int} - \mu\hat{N}_{electron} \\ &= -t\sum_{\langle i,j\rangle}\sum_{\sigma=\uparrow,\downarrow}(c^{\dagger}_{i\sigma}c_{j\sigma} + c^{\dagger}_{j\sigma}c_{i\sigma}) + U\sum_{i} n_{i\uparrow}n_{i\downarrow} - \mu\sum_{i}(n_{i\uparrow} + n_{i\downarrow})\ ,\end{aligned} \tag{2.4.1}$$

where $c^{\dagger}_{i\sigma}$ and $c_{i\sigma}$ are creation and annihilation operators of electrons with spin σ localized in an orbital at site $i \in 1, 2, ..., N$ of the lattice, and $n_{i\sigma} = c^{\dagger}_{i\sigma}c_{i\sigma}$. The symbol $\langle i, j\rangle$ emphasizes that hopping is allowed only between sites i and j which are nearest neighbours. The factors U and t are real numbers, which set the energy scale and fix the relative strength of them in the Hamiltonian. Their relationship to each other determines the metallic/insulator behaviour of a solid. $t > 0$ has a negative sign, because according to Heisenberg uncertainty principle, the electrons minimize their kinetic energy through delocalization, i.e. hopping between the atomic sites lowers the energy. The third term takes into account that the number of fermions changes and with that changes the local single-particle energy level with the constant chemical potential μ. Therefore, the role of μ is to control the filling n on the sites. Later on the half-filling (one electron per site for the single-band model) will be necessary to enforce the particle-hole symmetry in the material which describes the the Mott-Hubbard metal-insulating transition, see Sec. 2.4.3.

2.4.2 Single-Site and Non-Interacting Limits

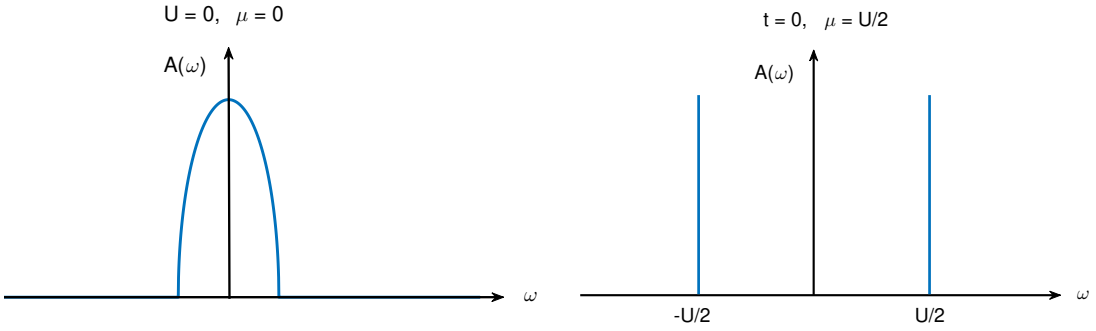

Figure 4: Schematic spectral functions in the non-interacting limit $U = 0$ (left) and atomic limit $U/t \to \infty$ (right), adapted from [18].

In order to get a more in-depth knowledge of the behaviour of strongly correlated electrons on a lattice, we will discuss the two main limits of the Hubbard model. The electrons hopping to neighbouring sites lowers the energy, however if there are two electrons on the same site, they experience a repulsion of strength U, which is energetically not favourable, hence the competition between the kinetic and the local interaction parts in the Hamiltonian. This correlation also shows how much the interaction term U influences the overall movement of the electrons and how it gives rise to profound quantitative and qualitative changes of the physical properties of electronic systems as compared to non-interacting particles. In the first limit, called the single-site limit, the electrons are localized, that is, the hopping from site to site is suppressed. This constraint can be achieved by making the interaction term large in comparison to the kinetic term: $U/t \to \infty$. But not only the proportion U/t affects the conductivity of a solid, so does the filling factor of the lattice $\langle n\rangle = N_e/N_l$ as well. Here the ratio of the number of electrons and the number of lattice sites gives the average filling of a site. In order to see how the filling affects the conductivity, consider a solid with the average filling of $\langle n\rangle = 2$. In this case the single-band is full and the conduction electrons cannot hop from one site to another, because

it is restricted by the Pauli principle. At half-filling $\langle n \rangle = 1$, the ratio of the interaction and kinetic term has a relevant impact on the physical behaviour of the material. In the single-site limit due to the strong Coulomb interaction, it costs too much energy for an electron to hop on a site with an extant electron on it. Therefore there are no freely moving electrons and the solid is in its insulating state, namely the *Mott insulator*. In order to calculate the actual form of the spectral function for the limits, we can use the Lehman representation from (2.1.10) and considering the four eigenstates for a single-band site with the corresponding energies from the Hubbard Hamiltonian with $t = 0$ (shown in Fig. 4, right),

$$A_\sigma(\omega) = \frac{1}{2}\Big(\delta(\omega - U/2) + \delta(\omega + U/2)\Big)\,. \tag{2.4.2}$$

As we can see, there are two $\delta-$peaks in the atomic limit at $\omega = \pm U/2$, contributing to the Hubbard bands. Between these excitations we find the Mott gap with the width of U and since the Fermi energy lies within the gap, in the atomic limit we find the Mott insulating phase.
Investigating the other extremity, $U/t \to 0$, we find the non-interacting limit, where the solid behaves like a Fermi gas. Here the kinetic term takes over and the interacting term is suppressed which means that the electrons can move around without any restrictions imposed by the Coulomb repulsion. Consequently, they are fully delocalized and they create a proper conduction band, that is, in the non-interacting limit the solid is in its metallic state. The spectral function of this case comes from the same calculation like for the single-site limit, but in the Hubbard Hamiltonian one sets $U = 0$ (shown in Fig. 4, left),

$$A_{loc}(\omega) = \sum_{\mathbf{k}} A_\sigma(\mathbf{k}, \omega) = \frac{1}{N}\sum_{\mathbf{k}} \delta(\omega - \epsilon_{\mathbf{k}}) = \rho_0^{Bethe}(\omega)\,, \tag{2.4.3}$$

where N is the number of electrons and the density of states $\rho_\sigma(\omega)$ has a semi-elliptical form for the Bethe lattice (2.1.28). At any other filling n, for a finite t the solid cannot reach an insulating state, since there will always be doubly and singly occupied lattice sites in the same time, which means that the hopping stays as a possibility to lower the total energy of the system.

2.4.3 Mott-Hubbard Metal-Insulator Transition

We previously discussed how the strongly correlated electronic systems in the two main limits look like. But the following questions arise, what happens between these two ends and how do the physical properties of a solid change. The transition between the metallic and insulating state (MIT) is called the *Mott-Hubbard transition*. Since the system always strives for a stable equilibrium state, which is equivalent to the state of the lowest total energy, a competition appears between the kinetic and correlation energies. This competition leads to the Mott-Hubbard transition between the two separate states - that is, between the itinerant and localized character of electrons in the material. To be able to describe this process, one needs to look at the variation of the local density of states (DOS) - or with other words the spectral function - as the ratio of the correlation strength U to bandwidth W (and to t) increases (Fig. 5). The hopping amplitude t of the Hubbard models is related directly to the the bandwidth W. For instance, on the Bethe lattice at zero temperature the bandwidth is $W = 4t$ [14]. The narrower the band the longer an electron stays on an atom and therefore it implies stronger correlation. The part of the spectral function close to the Fermi energy $\omega \approx E_F = 0$, is referred to as the *quasiparticle peak*, while the high-energy part forms the *Hubbad bands*. For $U/t \to \infty$, there are no quasi-particle excitations at $\omega \approx 0$ and thus the peak in the middle vanishes. If there is a finite value for the density of states at the Fermi energy then the solid is metallic, which also applies to the multi-band Hubbard models. Increasing the Coulomb interaction parameter between the electrons with respect to the hopping amplitude t (or bandwidth W) the solid goes through the Mott-transition and the density of states at the Fermi energy is exactly 0. If the spectral function vanishes at E_F that means that there are no excitations for the outer lying electrons or holes, i.e. the material is insulating.

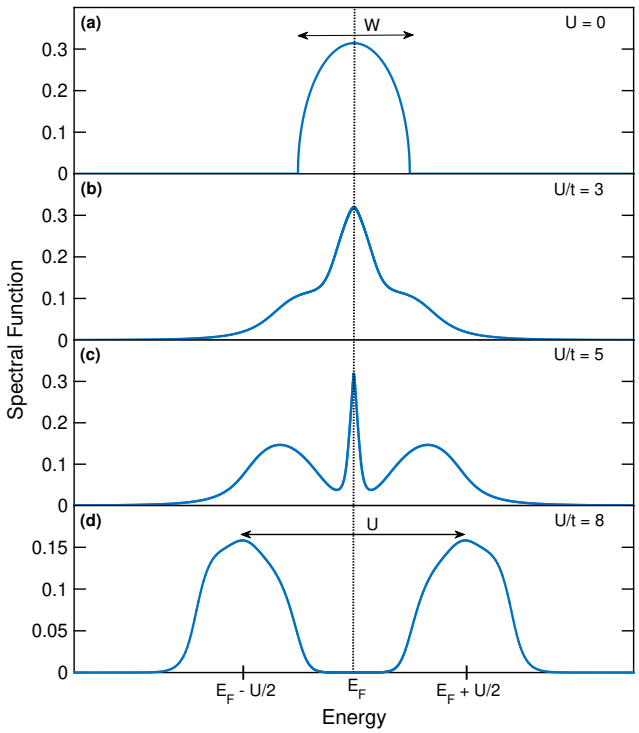

Figure 5: Schematic spectral functions of the single-orbital Hubbard model in a strongly correlated material as they go through the Mott transition, adapted from [32]. In (a) we can see the metallic phase in the non-interacting limit with the bandwidth W, which is equal to $4t$ for the Bethe lattice; (b)-(c) increasing the Coulomb interaction energy U lowers the quasi-particle weight (peak at the Fermi energy E_F) until it vanishes and leaves behind two separate Hubbard peaks (d), which is the characteristic spectral function of the Mott insulating phase.

2.4.4 Multi-Orbital Hubbard Model

Many of the materials that show a metal-insulator transition, have a multi-orbital structure. But considering more orbitals leads to new possible on-site interaction integrals, thus the single-band Hubbard model is not sufficient to describe most of the materials. Let us extend the model to the multi-band case, where the additional properties of the materials are understood via the Hund's coupling. In the following (with the MIT in mind) we will consider three-bands, where each energetically degenerate band contributes with two electrons to the strongly correlated system. In order to construct the extended version of the Hubbard Hamiltonian (2.4.1), one needs to consider a generalized hopping- and interaction matrix. The first one is easier to accomplish, it needs to contain the possible hopping amplitudes between the intra- and inter-orbital cases. For the rest of the dissertation we take a diagonal kinetic matrix, i.e. the hopping amplitudes among different orbitals are neglected. (But with this simplification a part of the orbital character of the model is lost.) On the other hand finding the more general interaction term for the multi-orbital model is not so straight forward. We will stick to the approximation of a local Coulomb interaction, i.e. it is only considered between the electrons on the same site. In the following equation we will see that the 'intra-orbital' repulsion (which we will refer to as the Hubbard interaction U_H) stays the same as in (2.4.1) but a new 'inter-orbital' interaction integral U appears,

$$U_{mm'} = \int d\mathbf{r}\, d\mathbf{r}' \phi^*_{im\sigma}(\mathbf{r}) \phi^*_{im'\sigma'}(\mathbf{r}') \frac{e^2}{|\mathbf{r}-\mathbf{r}'|} \phi_{im'\sigma'}(\mathbf{r}') \phi_{im\sigma}(\mathbf{r}) \Rightarrow \begin{cases} U_{m=m'} = U_H \\ U_{m\neq m'} = U \end{cases}, \qquad (2.4.4)$$

where the field operators of the electrons $\psi_\sigma(\mathbf{r})$ have been expanded via the low-energy Wannier wave functions $\phi_{im}(\mathbf{r})$ corresponding to the orbital m and site i,

$$\psi_\sigma(\mathbf{r}) = \sum_{im} \phi_{im}(\mathbf{r}) c_{im\sigma} \,,$$

with the fermionic annihilation operator $c_{im\sigma}$ [33]. Now we have to determine the additional interaction terms, which are essential to be able to describe any type of multi-band models well. At the results, we will see how much of an effect this new parameter has on both the three-fold and two-fold degenerate (or crystallic) multi-orbital Hubbard model. The inter-orbital Coulomb interaction (or Hund's coupling) is given by,

$$J_{mm'} = \int d\mathbf{r}\, d\mathbf{r}' \phi^*_{im\sigma}(\mathbf{r}) \phi^*_{im'\sigma'}(\mathbf{r}') \frac{e^2}{|\mathbf{r}-\mathbf{r}'|} \phi_{im\sigma'}(\mathbf{r}') \phi_{im'\sigma}(\mathbf{r}) \,. \tag{2.4.5}$$

In these Coulomb integrals J is also approximated to be screened, i.e. all the interaction amplitudes between the sites i and j are neglected. Earlier, for the spectral functions and density of states we used the Bethe lattice, because of its useful properties. Now, just for the introduction purposes, we take a cubic lattice and its three, degenerate orbitals on the d-level, labelled as t_{2g}. With the Hund's coupling J, the many-body Kanamori Hamiltonian can be formulated for the degenerate orbit-triplet (t_{2g}) states [34],

$$\begin{aligned} H \;=\; & \sum_{\substack{\langle ij \rangle \\ mm'\sigma}} t_{ij}^{mm'} c^\dagger_{im\sigma} c_{jm'\sigma} - \mu \sum_{im\sigma} n_{im\sigma} + U_H \sum_m n_{m\uparrow} n_{m\downarrow} + U \sum_{m \neq m'} n_{m\uparrow} n_{m'\downarrow} + \\ & + (U-J) \sum_{m<m',\sigma} n_{m\sigma} n_{m'\sigma} - J_X \sum_{m \neq m'} c^\dagger_{m\uparrow} c_{m\downarrow} c^\dagger_{m'\downarrow} c_{m'\uparrow} + J_P \sum_{m \neq m'} c^\dagger_{m\uparrow} c^\dagger_{m\downarrow} c_{m'\downarrow} c_{m'\uparrow} \,, \end{aligned} \tag{2.4.6}$$

where $U_H = U - J$, $J_X = J$ and $J_P = 0$ are adopted conventions to recover maximal spin- and real space rotational invariance of the Hamiltonian. (Note that it differs from the convention often used in Monte-Carlo calculations, where $U_H = U + 2J$ and $J_P = J$.) This retained invariance is believed to reflect the physics of the system well. (2.4.6) ensures that the Hund's rules are incorporated as the orbitals are filling up with electrons. The inter-orbital Coulomb interaction is the lowest for identical spins $(U-J)$ which is followed by the second lowest energy, the inter-action between different spins (U). It is not energy efficient for the electrons to be in the same orbital so as they fill up the site, hence they distribute among the orbitals according to the Hund's rules: 1) maximizing the total spin S, 2) given the spin S, maximizing the total angular momentum L and 3) selecting the lowest $J = |L - S|$ for a less than half-filled shell and the highest $J = L+S$ for more than half-filled shell. But due to its complicated nature this last rule is not accounted for in the above introduced Hamiltonian. The last two terms in the Hamiltonian (2.4.6) also contribute to the rotation invariance of the Hamiltonian, they are related to the spin-flip and pair-hopping processes respectively. But for our computations the pair-hopping is neglected by using $J_P = 0$. Later we will see how much the Hund's coupling affects the Mott transition and the critical interaction values, while recovering some of the qualitative results of the papers [35, 36, 37, 38, 39, 40]. The ratio of the two interaction terms U and J is also important, concerning the physics of the system. As in [41] somewhat discussed, the condition $U > 3J$ (which is fulfilled most of the time in our computations) ensures that the Hubbard interaction U controls the occupancy mostly and only after that J controls the arrangement of the electrons among orbitals. For $U < 3J$ it is the other way around and the system tries to maximize the total spin first and then adjust the local occupancy. The latter type of the strongly correlated systems has not been relevant.

2.4.5 Crystal Field Splitting

So far we have investigated the physics of the single-orbital and the fully degenerate multi-orbital Hubbard model, for which all three orbitals have the same energy level $\varepsilon_1 = \varepsilon_2 = \varepsilon_3$. Since in many of the crystals the electron orbitals differ from each other, the assumed orbital-symmetry does not reflect the reality well enough [42, 43, 44]. For the simplest crystal field splitting we consider two degenerate orbitals with $\varepsilon_2 = \varepsilon_3$ and one separate orbital with a different energy level ε_1. For such a case, a new characterizing parameter has to be introduced, the crystal splitting parameter $\Delta \equiv \varepsilon_1 - \varepsilon_2$. Shifting the energy levels changes the Hubbard Hamiltonian to

$$H = \sum_{\substack{\langle ij \rangle \\ mm'\sigma}} t_{ij}^{mm'} c_{im\sigma}^{\dagger} c_{jm'\sigma} - \sum_{im\sigma} (\mu - \Delta_m) n_{im\sigma} + \sum_i H_{loc}^i \,, \tag{2.4.7}$$

where m, m' and σ represent the orbitals and spins on the neighbouring sites $\langle ij \rangle$. The non-diagonal kinetic matrix elements are assumed to be zero, thus only the hopping between the same orbitals $m = m'$ of different sites contributes to the kinetic energy. H_{loc}^i stands for all the screened Coulomb interactions within and among the orbitals on site i. The crystal splitting (or the orbital asymmetry) is implemented in the second term by Δ_m, which will be set for the orbitals $m = 1, 2, 3$ as the following: $\Delta_1 := +\Delta/2$, $\Delta_{2,3} := -\Delta/2$. Using the DMFT approximation, one finds the self-consistent solution of a quantum impurity model given by the Hamiltonian

$$H_{imp} = -\sum_{m\sigma} (\mu - \Delta_m) n_{m\sigma} + H_{loc} - H_{hyb} - H_{bath} \,, \tag{2.4.8}$$

where the H_{bath} and H_{hyb} terms remain the same as in the SIAM Hamiltonian (2.1.19). There are two possibilities to choose the crystal splitting parameter, one where Δ is positive which will be referred to as the 1-up, 2-down shifting. The other one, when Δ is negative, is the 1-down, 2-up shifting. It is important to distinguish these two cases, because as the observations show, both have different physics. In our context the average occupation is fixed to $\langle N \rangle = \sum_{m=1}^{3} \langle N_m \rangle = 2$ with $\langle N_m \rangle \equiv \sum_\sigma \langle c_{m\sigma}^{\dagger} c_{m\sigma} \rangle_T$. In the atomic limit for $\Delta = 0$ the energetically favoured ground-states are $(|0\rangle, |\uparrow\rangle, |\uparrow\rangle)$, $(|\uparrow\rangle, |0\rangle, |\uparrow\rangle)$ and $(|\uparrow\rangle, |\uparrow\rangle, |0\rangle)$, where the vector components represent the orbitals $m = 1, 2, 3$ respectively. Since we are dealing with the superposition of these possible ground-states, the average occupation of each orbital at the same energy level is $\langle N_m \rangle = 2/3$.
Let us first consider the positive crystal splitting $\Delta > 0$ at filling $\langle N \rangle = 2$. Shifting the non-degenerate orbital up means that staying on it is energetically less advantageous for the electrons and they move to lower-lying degenerate orbitals. (Note that at half-filling $\langle N \rangle = 3$, the correlated system would behave differently due to the Hubbard interaction U_H in the same orbital. The third electron would not necessarily jump down to the lower-lying bands because of the Coulomb repulsion.) If we lift the separate orbital to a higher energy level the electron occupation will shift to the lower levels. Similarly, for a constant field splitting and continuous increase of the interaction U will lead to the same result: the electrons move from the higher level to the lower one until the non-degenerate orbital depletes. This tendency can be reasoned by the decrease of the kinetic energy: as the potential energy increases the hopping onto the site becomes more difficult and the electrons does not distribute to all three orbitals. Instead, they choose the energetically favourable lower-lying orbitals. At a certain U_c^{occ}, the interaction becomes large enough that all the electrons move to the lower bands $m = 2, 3$, which means that the upper band $m = 1$ is empty and hence it is a band-insulator. On the other hand the degenerate double-band is half-filled with the given two electrons. One of the aspects of the Hund's coupling is that at half-filling it lowers significantly the critical interaction values U_c^{23} [45], which can lead to $U_c^{23} < U_c^{occ}$, i.e. the interaction (which is needed to achieve half-filling on the double-band) is strong enough to make the electrons localized and the degenerate double-band is Mott-insulating. The other possibility is when $U_c^{23} > U_c^{occ}$, which means that the half-filled bands $m = 2, 3$ stay metallic, while the empty single-band is in a band-insulating phase.
The other case, with negative crystal splitting $\Delta < 0$, behaves differently. Here the two degenerate bands $m = 2, 3$ are shifted to a higher -, while the separate band $m = 1$ is shifted to a lower energy level (2-up, 1-down). The starting occupations are the same as before and the tendency is similar as well, i.e. the electrons move to the lower-lying energy band. However, the higher-lying bands do not deplete entirely, because in this case there would be two electrons on the non-degenerate single-band, thus a strong Coulomb repulsion would come into action,

which is energy-costly. Correspondingly, with the increase of U the electron orbital-occupation shifts until the number of electrons becomes 1-1 for the lower band (half-filling) and for the higher bands (quarter-filling), respectively. To achieve this divided occupation the earlier used argument with the decreasing kinetic energy due to the increasing interaction, applies again. Thus via the hybridization of the impurity, the system gains less energy as U becomes stronger. If the 1-1 occupation is achieved then an interesting phenomenon can be observed. It can occur that for the same interaction parameters (U, J), the degenerate orbitals are in a different phase than the unique orbital, which is called the *Orbital-Selective Mott Transition* (OSMT). In this case the material is neither a perfect metal nor a perfect insulator. It has the capability of conducting electrons but there are still many strongly correlated, localized electrons. The condition for the occurrence of the OSMT is that the two-orbital and single-orbital critical interactions are not equal at the reached filling. Both the orbital-degeneracy (since it increases the kinetic energy [46, 47]) and the Hund's coupling at non-half-filling [45] increases the critical interaction, which leads always to OSM-phases with $U_c^1 < U_c^{23}$ where the double-band is metallic and the single-band is Mott insulating. It is also important to note that the Hund's coupling J plays the role of a stabilizer of the OSMT. J has to be sufficiently large to decouple the bands from each other and to suppress the fluctuation among the bands. Thus, if $J \to 0$, the solid would go through a normal Mott transition without any orbital-selective aspect [44].

3 Results and Discussion

In this section we will discuss various results of the phase diagrams of the Hubbard model. First of all we are interested in the critical values of the interaction term U, where the Mott-Hubbard metal-insulator transition occurs. But the critical values U_c depend on the direction of the phase transition, i.e. the critical values are different for the metal-insulator and the insulator-metal transition. As we have previously seen, a characteristic property of the metallic phase is the quasi-particle peak at $\omega = 0$. If there are excitations at the Fermi energy (at $E_F = \mu := 0$ for $T = 0$) then the system is metallic. On the other hand if the Fermi energy level lies in a Mott gap between the Hubbard bands, i.e. the spectral function vanishes at $\omega = 0$, then the system is insulating. Now, if there is a metallic input hybridization and the interaction term U is increased, then reaching $U = U_{c2}$ the system goes through the MIT transition and the electrons become localized. Similarly, for an insulating input and a decreasing U, the transition appears at a lower critical value $U = U_{c1} < U_{c2}$ for which the electrons become delocalized. The interval $U \in [U_{c1}, U_{c2}]$ is called the *hysteresis*, where both states fulfil the DMFT self-consistency condition but one of them might have a lower total energy. Theoretically we handle the system in the limit of infinite dimensions and at zero temperature. With respect to these conditions the transition between the metallic and insulating phases becomes continuous [48], i.e. the quasi-particle weight vanishes smoothly by increasing the interaction. A large electronic system however leads to numerical difficulties, which is the reason to treat the system in the limit of infinite dimensions and thus making the complicated structure of the DMFT numerically more tractable. Also, considering finite temperatures could significantly change the character of the phase transitions and thermodynamic quantities. For instance the influence of the temperature on the Hund's rule exchange term J is discussed in [49].
The most critical point of the calculations is the Numerical Renormalization Group, which computes the local self-energy for an input hybridization iteratively. The implemented code was provided by the group of Jan von Delft at the Chair of Theoretical Solid State Physics at Ludwig-Maximilian-Universität München. It is based on the QSpace library [50] developed by Andreas Weichselbaum. The code can be used to calculate spectral functions even for arbitrary temperatures [51] and to deal with three-band Hund's metals as well [52]. Its advantage is that it provides real-frequency solutions for the low energy spectrum (near the Fermi energy), while this is more difficult to achieve with other methods, such as the Quantum Monte Carlo (QMC) methods [53].

3.1 Single-Orbital Mott Transition

In order to understand all the elements and characteristics of the spectral functions, critical interaction values and phase diagrams, let us first discuss the single-orbital case at half-filling. This filling condition enforces the particle-hole symmetry, which leads to symmetric spectral functions, i.e. there are as many particle excitations as hole excitations, see Fig. 6. Here we can also see how the strength of the interaction influences the spectral functions. For the insulator input (Fig. 6 (a)-(b)), as the Coulomb repulsion decreases, so does the width of the Mott gap. The two separate peaks approach each other as the correlation weakens and the gap between them vanishes at U_{c1}, hence it is the insulator-metal transition. Within the metallic phase (Fig. 6 (c)-(d)), the quasi-particle peak in the middle gets narrower as the repulsion between the electrons becomes stronger. At U_{c2} the metallic peak vanishes and the Fermi energy is in the Mott gap, hence it is the metal-insulator transition. Note that the critical values U_c have a temperature dependence, but it will not be discussed in this dissertation, since we take the same temperature for every calculations. More details on the finite temperature Mott transitions can be found at [54, 55]. Let us now take a metallic initial phase in the hysteresis, i.e. $U_{c1} \leq U \leq U_{c2}$. In order to be able to argument that the solid is in a certain phase, the DMFT self-consistent calculations has to converge for the given MIT parameters. The error margin is set to $\epsilon_{hyb} = 10^{-4} - 10^{-3}$, that is, the last output hybridization does not differ from the last input hybridization more than the margin. For the single-band we enforced the half-filling and during the computations the value of the occupation stays constant. However, later on for the more complex multi-band model the occupation deviates from the input filling $N = 2$. Therefore, the convergence is only achieved if the fluctuation of the average occupation does not overcome an error margin, which is usually set to $\epsilon_{occ} = 10^{-4}$. In the hysteresis the convergence is difficult to achieve and one

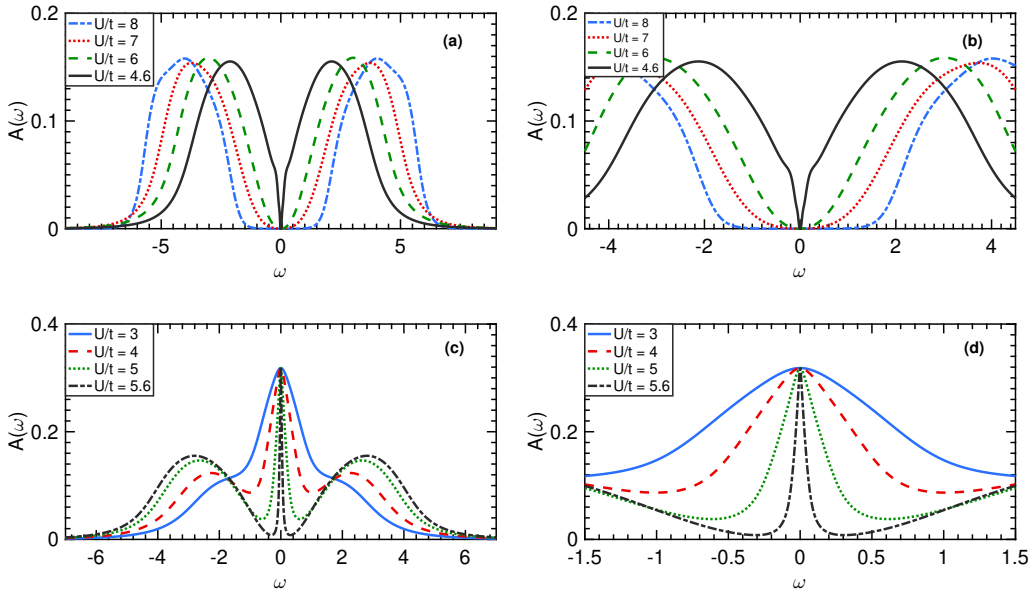

Figure 6: Spectral functions of the insulating (a,b) and metallic single-band phases (c,d) at half-filling ($N = 1$) as they are approaching the Mott transition critical point. Figures (c) and (d) are the zoomed in versions respectively. Near to the critical interaction both the Mott gap (b) and the FWHM of the quasi-particle peak (d) becomes narrower.

has to improve the accuracy of the computations. This can be done by enhancing the NRG iterations within the DMFT by (i) increasing the number of retained many-particle states and respectively raising the level of the rescaled truncation energy (for the single-orbital case around 1000-3000 multiplets, and $E_{trunc} = 8$), (ii) decreasing the discretization parameter Λ (usually $\Lambda \approx 2$, note that for $\Lambda = 1$ the continuous bath spectrum would be recovered),(iii) applying z-averaging ($z = 2 - 4$) or (iv) simply increasing the number of DMFT iterations (it is usually varied from 25 to 100). All of these changes however lead to longer computations, which for the single-band case is still not a problem, but the multi-band model can take many days to achieve convergence.

Let us now determine the exact critical interaction values U_c of the Mott transitions quantitatively for the simplified single-band system. The results will also serve as an indicator where the possible Mott transitions can occur for the multi-band models as well and comparing them to each other will give us a better understanding how the strongly correlated systems work. For both type of input hybridizations, we used the same principle to determine the critical interaction values U_c. After many computations with different interaction strength U, we saw that for the insulating seed the first converged metallic phase was achieved at $U_{c1} = 4.10t$. On the other hand, taking a metallic seed, the first data for which a converged insulating phase occurs is at $U_{c2} = 6.70t$. As the system approximates to the critical value U_{c1} (and U_{c2}) the width of the gap (and of the quasi-particle peak) approaches to zero, see Fig. 7. If we take the width of the Mott gaps for the last insulating phases and then extrapolate linearly (following the thought process of [56]), we receive $U_{c1} = 4.24t$ for which the gap vanishes. The full width at half maximum (FWHM) of the quasi-particle peak in function of the interaction U disappears (using the same method) at $U_{c2} = 6.62t$. Note that our calculations could only use the data near the critical values U_c. Points further away also seem to change linearly but with a different incline. Approaching the critical values, makes it more and more difficult to receive converged hybridizations because the output becomes unstable, which leads to larger errors in every iteration of the NRG and DMFT computations. A crucial factor that can lead to deviations is the number of kept states in the NRG iterations (and also the fineness of the logarithmic discretization of the continuous bath spectrum). The more states we cut off to fix the Hilbert space the more possible it is that the resulted metallic or insulating phase is not the actual phase of the solid. We have written down at which interactions did the computations reach a convergence. However, if we had taken a larger amount of states to be kept in the calculations, these results might be different. The

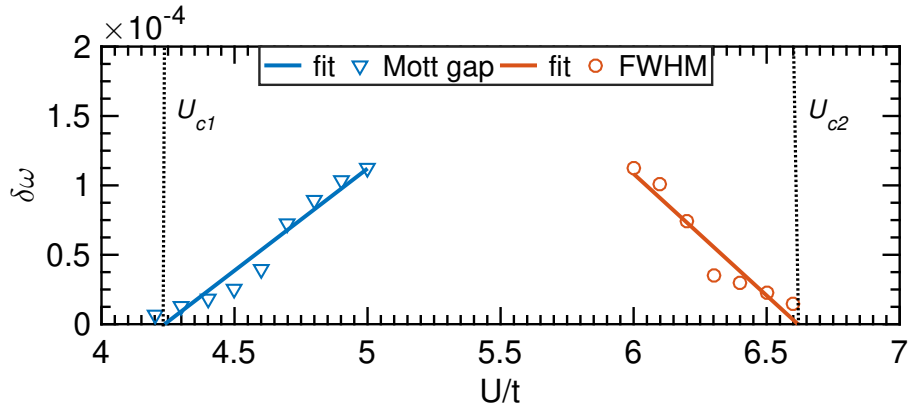

Figure 7: The decrease of the FWHM for the metallic phase and the width of the Mott gap for the insulating phase while approaching the critical interaction values U_c, can be linearly extrapolated to get a quantitative result for U_{c2} and U_{c1}.

reason is, that although we know that the states with higher energy do not influence the lower energy physics significantly, we can still neglect important states which do affect the outcome of the spectral function. The fits on the peaks in order to calculate the actual gaps and widths, are not perfect either. The reason can be that both lengths become as small as 10^{-5} and the form of the spectral function becomes quite complicated while approaching the transition interaction. Consequently, it becomes difficult to find a well fitted Gaussian peak for the Hubbard band peaks or for the quasi-particle peak. This can explain the deviations from the literature values, which are around $U_{c1} = 4.74t$ and $U_{c2} = 5.82t$ [56]. That is, the size of the hysteresis is smaller for the literature values. In general, we have also observed that by enhancing the accuracy of the NRG computations the gap between the critical interactions U_{c1} and U_{c2} decreases.

3.2 Multi-Orbital Phase Diagram

The extended Hubbard Hamiltonian (2.4.6) to the degenerate multi-band model incorporates all the new elements of both the kinetic and interaction terms of the system. Since the multi-orbital model is more complicated than the signle-orbital one, it is crucial to enhance the accuracy of the NRG computations for the desired converged spectral functions. Because the Hilbert space grwos even faster exponentially for three-orbitals the logaritchmic scaling parameter had to be increased to $\Lambda = 8$. The number of kept states were also raised to 3000-5000 multiplets. The Mott transition for degenerate bands takes place at any given integer filling [41] (not just at half-filling, which was required for the single-band). Furthermore, U_c is the smallest at half-filling and becomes larger moving away from it. There is a significant distinction between the integer fillings $N = 1, 2$ and the half-filling $N = 3$. If a fourth electron hops onto the atomic site with half-filling, due to the on-site spin polarization constraint, the electron has to go through a spin flip process which leads to a much wider Mott gap than for the other integer filling cases. In principle, the boundaries of the phase transition and with that the Mott gap can be described by taking the atomic limit [45]. Let E_n denote the lowest eigenenergy of H_{loc}, then the Mott gap can be approximated as the following,

$$\delta\omega(n) = E_{n+1} + E_{n-1} - 2E_n \,. \tag{3.2.1}$$

The actual Mott gap is just shifted by the order of the bandwidth. Setting J to zero, the local interaction Hamiltonian becomes $H_{loc} = UN(N-1)/2$ and that yields the Mott gap $\delta\omega = U$. In general, $J \neq 0$, $\delta\omega(1) = \delta\omega(2) = U - 3J$. But thus the spin flip of the fourth electron added to the site, the Mott gap for half-filling $N = 3$ becomes $\delta\omega(3) = U + 4J$. These theoretical results show a two-sided effect of the Hund's coupling [45]. On the half-filled sites, a non-vanishing J prevents the low-energy electrons to become conducting with a wider Mott gap, thus enforcing an insulating phase. That is, by increasing J at half-filling, decreases the critical interaction values, required for the Mott transition. On the other hand, for the integer fillings $N = 1, 2$, the orbital fluctuations contribute to a narrower insulating gap, which makes it more possible for the electrons to be part of the conduction band. Thus increasing J leads to an increased

U_c. Note that this is not the tendency if we start from a non-Hund correlated system, $J = 0$. Here, the introduction of the Hund's coupling to the system with $J > 0$ results first in a decrease of the critical interaction (see Fig. 10). The reason is that for a weak Hund's coupling $J < t$ the quasi-particle weight decreases and with it the conductive nature weakens in comparison to $J = 0$, hence for the Mott transition the needed critical interaction first becomes lower [57, 58]. In the computations, we examined the Mott transitions always at the filling $N = 2$, apparently the system responds more evidently for varied Hund's coupling and crystal shifting at this exact filling. The chemical potential μ is adjusted dynamically to fulfil the total on-site occupation number condition (N = 2). We will use the initial guess, $\mu = -3/2(U - J)$ [59].

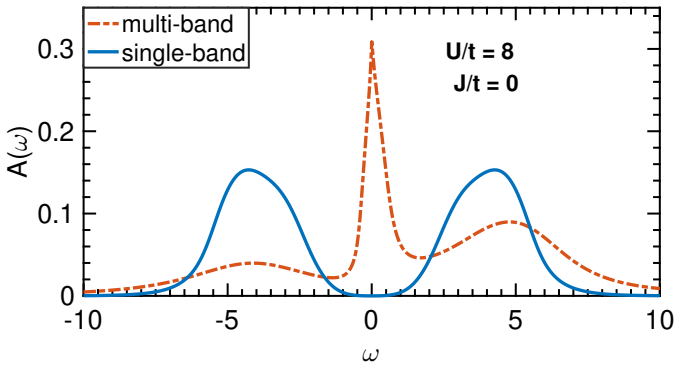

Figure 8: Spectral functions of the single- and multi-orbital Hubbard model ($J/t = 0$) at the same interaction $U/t = 8$. It shows that the critical value U_{c2} is in general increased for a multi-orbital system even though the Hund's coupling is neglected $J/t = 0$. At $U/t = 8$ the single-band model already went through the Mott transition, i.e. it is an insulator, while the multi-orbital model stays in its metallic phase. In the latter case, for the phase transition a much stronger interaction would be needed, around $U/t = 13$. Note that the multi-band spectral function shows one of the degenerate multi-bands and not the combination of two, thus a *direct* comparison between the single-band and multi-bands is not possible.

In general the Hund's coupling modifies the energetics of the system, i.e. both the critical values U_c and the shape of the spectral functions are modified. But first of all let us investigate how the degeneracy of the bands with $J = 0$ (i.e. $U = U_H$) affect the Mott transition and compare it to the single-band case. Both of the spectral functions are shown in Fig. 8. The critical Coulomb interaction parameter U_c increases with the orbital degeneracy for $J = 0$, due to the bands' increased kinetic energy [46, 60]. With other words, for the same value of U in an initial metallic phase, the single-orbital model can already be in its Mott insulating phase peak, while the multi-band model has not even approached the transition (Fig. 8). Variation in the strength of the screened Coulomb repulsions has the same effect on the phase transition as for the single-band model, i.e. both the quasi-particle weight for the metallic phase and the Mott gap for the insulating phase decreases while approaching U_c (Fig. 9 (a)-(b)). As we can see in Fig. 9 the spectral functions are asymmetrical with more spectral weight for positive

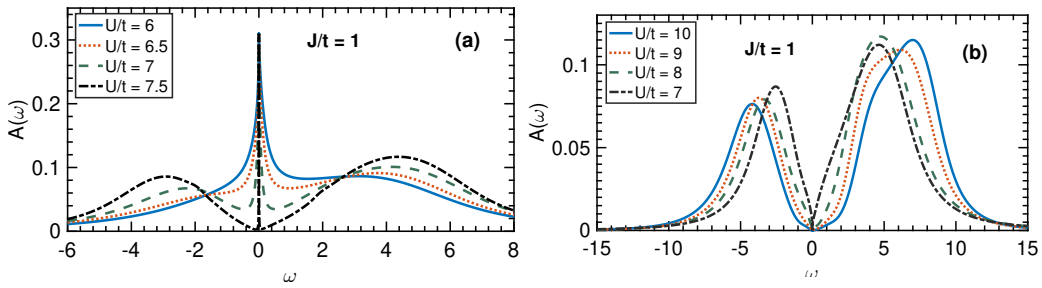

Figure 9: Spectral functions of the (a) metallic and (b) insulating phases as they are approaching the critical correlation U_c. Respectively, the width of the quasi-particle peak and of the Mott gap decreases.

energies $\omega > 0$. This reflects the filling $N = 2$ (particle-hole asymmetry), since there are more holes than electrons and thus there are more particle excitations than hole excitations. With the atomic limit, we can determine the positions of the main peaks of the multi-band model. There is only one type of hole-excitation which corresponds to the Hubbard peak on the left side of the spectral function. On the right side, contrary to the resulted figures there can be two separate particle excitation energies not just one, corresponding to the transitions $(|0\rangle, |\uparrow\rangle, |\uparrow\rangle)^T \rightarrow (|\uparrow\rangle, |\uparrow\rangle, |\uparrow\rangle)^T$ and $(|0\rangle, |\uparrow\rangle, |\uparrow\rangle)^T \rightarrow (|0\rangle, |\uparrow\downarrow\rangle |\uparrow\rangle)^T$. The latter one's energy is higher by the Hund's coupling J. But these peaks can be merged together because of the logarithmic scaling of the NRG discretization, which has the purpose to investigate the system near the Fermi energy $E_F \overset{T\rightarrow 0}{=} \mu \Leftrightarrow \omega = 0$ but at the expense of a coarse resolution at higher energies. Also, for weak interactions these excitation energies lie close together in the energy spectrum, but if the interaction is strong enough, the sub-peaks can be observed, see Fig. 9 (b) with $U/t = 10$.

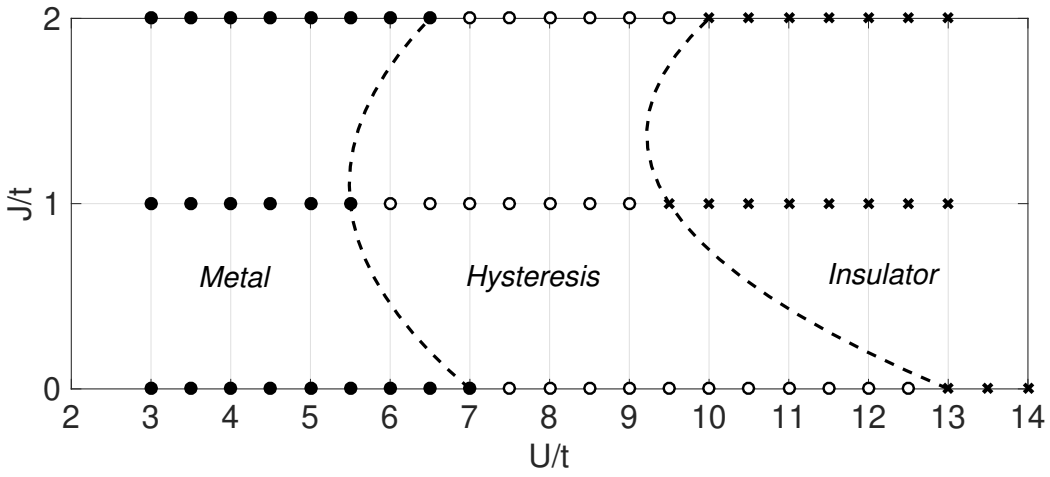

Figure 10: Phase diagram of the three-fold degenerate multi-orbital Hubbard model at the filling $N = 2$ on the $J - U -$ plane. The full -, hollow circles and the crosses denote the metallic, coexistent and insulating phases respectively. The dashed lines are supposed to represent the presumed boarders of the M-I and I-M transitions. Between the boarders, in the hysteresis there are coexistent phases, both metallic and insulating.

In contrast to the single-orbital model, the Mott transition in the degenerate multi-orbital model has U and also J dependence. The phase diagram (Fig. 10.) was made to represent the metallic, insulating and coexistent phases for certain (U, J) points. In general, the exchange coupling $J \neq 0$ increases the values of U_c at the filling $N = 2$, which has been also shown in various experiments [46, 58, 61]. This increase of U_c can be seen for $J \geq 1$ in the phase diagram. As previously discussed, the critical strength U_c is different if it is a metal-insulator (M-I) or an insulator-metal (I-M) transition. If the system starts in the metallic (insulating) phase, then it persists in staying in the initial phase, thus it needs a stronger (weaker) correlation to enforce the Mott transition. Therefore $U_{c1} < U_{c2}$ and in between these values we find a coexistent regime of both metallic and insulating phases. The last metallic and insulating points before the transition (full circles and crosses in Fig. 10.) outline the shape of the hysteresis in the $J - U -$ plane. All the points in the coexistent region are denoted by hollow circles. The phase diagram affirms our theoretical considerations and shows first a decrease in U_c between $J = 0$ and $J = 1$ and then an increase for $J = 2$. The curved nature of the dashed lines is a consequence of several computations for non-integer J values. However, the shape of the boarders are not computed in our figure, it only serves as a representation of the non-linear dependency [58].

3.3 Crystal Field Phase Diagram

In order to make our discussion of the Mott transition even more comprehensive, let us lift the three-orbital degeneracy by shifting the energy levels of the orbitals. In the previous section, due to the degeneracy, the MIT occurred for all the bands simultaneously. However, when one of the band's energy levels differs from the other two bands', then new physics appears for the system, which is worth to investigate. In the following we will discuss the results for two different crystal fields, one with a positive splitting $\Delta = +0.4\,t$ and one with negative splitting $\Delta = -0.4\,t$. For the latter one an interesting phenomenon can be observed: for the same MIT parameters the shifted bands can be in different phases, which case is called the Orbital-Selective Mott Transition (OSMT). Consequently, part of the electrons are itinerant and thus conductive while the rest of them are still localized to the sites and thus insulating. For instance, this orbital symmetry breaking is relevant for the Mott transitions in $SrRuO_3$, in which there is an average occupancy of $N = 2$ (the filling we consider as well). The simplest case of the symmetry breaking is described by the three-fold degenerate triplet cubic state t_{2g} splitting into a singlet and a doublet. Another way to lift the degeneracy of the orbitals is to choose different bandwidth, which would have similar effects as shifting the orbitals. When the OSMT occurs in a solid, one has to distinguish two phase transitions: (i) from metallic (M) to orbital-selective metallic (OSM) and (ii) from OSM to Mott insulating phase (MI). In the absence of the Hund's coupling or even for $J \lesssim 0.3$ the OSM phase entirely disappears [43]. If the site has in general a lower energy level by applying the crystal splitting, it means that the down-shifting creates place for a possible additional electron. That is, as the term $(\mu - \Delta_m)$ decreases, the occupancy of the down-shifted band(s) m are increased, while the occupancy of the up-shifted band(s) $m' \neq m$ are decreased. Since the crystal fields are even more complex then the fully degenerate three-orbital case, the accuracy of the NRG calculations had to be improved even more, otherwise there would have no convergence achieved for the hybridizations. We increased the number of kept states to 6000-8000 multiplets with $E_{trunc} = 9$ and the logarithmic scaling parameter was $\Lambda = 7 - 8$. These NRG parameters worked most of the times well for the crystal fields, but there were few critical cases where they could only approach convergence but could not reach it.

3.3.1 Positive Crystal Field Splitting

Let us handle the two different crystal fields separately and first look at the characteristics of the positive splitting $\Delta/t = +0.4$. For $\Delta > 0$ the single-band $m = 1$ is shifted up and the degenerate two-bands $m = 2, 3$ are shifted down (1-up, 2-down). Since the total number of on-site electrons in average is $N = 2$, at the beginning all three orbitals have the filling $n_m = 2/3$ (the kinetic energy prevents the second electron to be on the lower-lying double-orbitals). That is, the occupation vector yields $\vec{n} = (n_{m=1}, n_{m=2+3})^T$ with $n_{m=1} = 2/3$ and $n_{m=2+3} = 2 \cdot 2/3 = 4/3$. Consequently, both behave metallic for weak interactions, see Fig. 11 (a). In the figure we can also observe that the double-band's spectral weight on the left side (particle-side) is larger than it is for the single-band. Since shifting the two-fold degenerate bands down makes them energetically more favourable, one would first assume that for an arbitrary small (but non-vanishing) crystal splitting both the electrons would start on the lower-lying double-band. But the kinetic energy via the hybridization of the impurity with the surrounding bath is lower if the electrons are

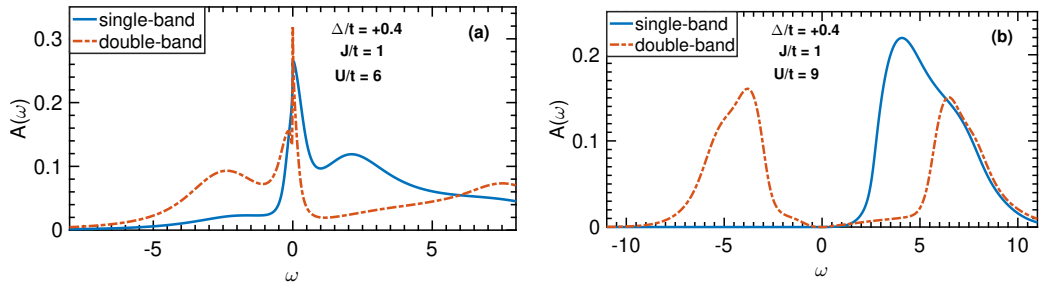

Figure 11: Spectral functions of the (a) metallic and (b) insulating phases of the multi-band Hubbard model with positive crystal field splitting $\Delta/t = +0.4$. In each figure, the spectral functions of both the single-band and one of the degenerate double-band are plotted for the same U and J parameters.

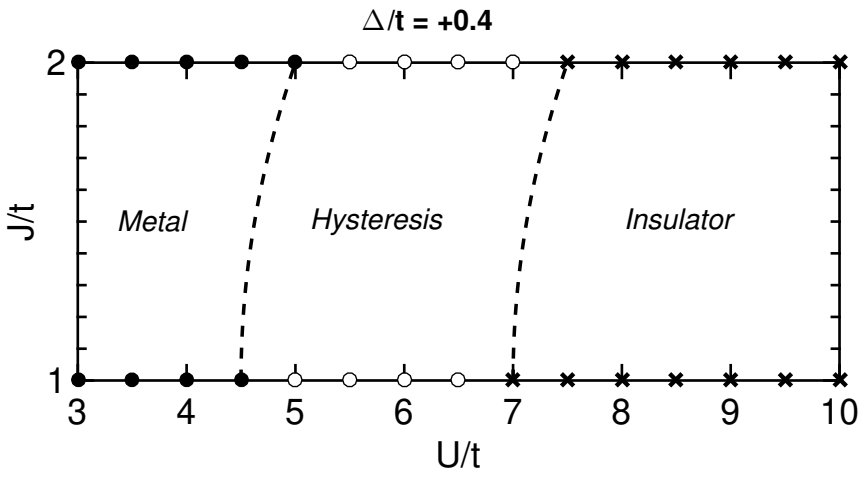

Figure 12: Phase diagram of the crystal field with positive splitting parameter $\Delta/t = +0.4$. Showing the different regimes on the $J - U-$plane, from left to right: metallic-, coexistent-(hysteresis) and finally the Mott insulator phases. Computed phases are labelled by full-, hollow circles and crosses respectively.

equally distributed to all three orbitals. This leads to an orbital occupations of $n_{2+3} < 2$ and $n_1 > 0$. As discussed in the theory section, if the interaction U gets stronger, the kinetic hopping becomes suppressed and thus the system does not strive for a three-orbital electron distribution any longer. That is, the electrons tend to be on the lower-lying double-band so the occupation vector becomes $\vec{n} = (0, 2)^T$ for strong interactions. The depletion of the single-orbital means that at this point it is insulating, see Fig. 11 (b) and since there are no electrons in the orbital the spectral function on the left side vanishes. In the same time the two-fold degenerate bands are half-filled and with $J \neq 0$ this separate system's critical interaction value is relative small [58]. Since the interaction had to be sufficiently large to achieve this end occupation of $(0, 2)^T$, the double-band will also be in its insulating phase. Fig. 11 (b) also shows a spectral function with similarly shaped Hubbard peaks for the particle and hole excitations (half-filled), but they are not entirely symmetric due to the Hund's coupling.
For a stronger CFS $1 < \Delta/t < 3$ the $(0, 2)^T$ occupation is reached for weaker interactions U. If this interaction is weaker than the critical value U_c^{23} then it is possible that the double-band is still metallic while the single-band is band-insulating. The Δ-dependency of U_c is also discussed at filling $N = 4$ in [62] (which is relevant for our case too, because $N = 2$ and $N = 4$ are connected via a particle-hole transformation). But for weaker crystal fields, which were investigated in this dissertation, such a hybrid phase (it is not an OSM-phase because the single-band is a band-insulator not a Mott insulator) is not possible for positive splitting. Thus in the phase diagram Fig. 12 the circles and crosses label the phases of both the single-band and double-band in the same time. Note that it is not reasonable to discuss the phases for $J = 0$ because the Hund's rule coupling term plays a key role as an orbital-decoupler in the crystal fields. Thus results for CFS with $J = 0$ have not been investigated. Comparing the phase diagram of the crystal fields to the phase diagram of the fully degenerate multi-orbital Hubbard model (Fig. 10), the hysteresis regime is shifted to the right, i.e. the Mott transition occurs for lower interactions if the orbital-symmetry is broken. This result is also verified by Fig. 1 in [62]. Since by increasing the interaction U more and more electrons shift to the lower-lying double-bands, the effective correlation becomes higher too. The effective interaction is responsible for the decrease of the quasi-particle weight [41], thus the critical interaction U_c where the quasi-particle weight fully vanishes, becomes smaller. The curved boarders of the hysteresis between $J = 1$ and $J = 2$ are once again only a representation of the qualitative observations that the critical value U_c increases non-linearly as the Hund's coupling term J is increased.

3.3.2 Negative Crystal Field Splitting

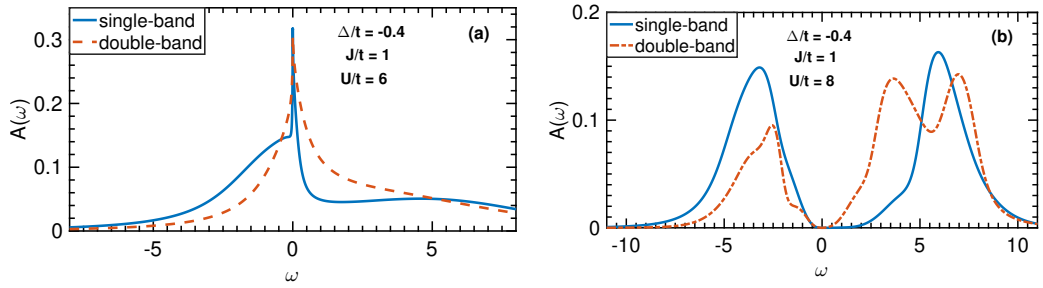

Figure 13: Spectral functions of the (a) metallic and (b) insulating phases of the multi-band Hubbard model with negative crystal field splitting $\Delta/t = -0.4$. In each figure both the single-band and degenerate double-band spectral functions are plotted for the same U and J parameters.

In this section, let us look at the 2-up, 1-down crystal fields at filling $N = 2$, with the negative splitting parameter $\Delta/t = -0.4$. The equal orbital-distribution applies to this crystal field too because of consequential lower kinetic energy. Hence for a starting metallic phase the orbital occupations are $2/3 < n_1 < 1$ and $n_{2+3} > 1$. This leads to a larger spectral weight on the left side for the double-band, see Fig. 13 (a). As the potential energy gets larger and hence the kinetic energy smaller, the electron occupation shifts to the lower-lying separate orbital. But since it is a single orbital, if there is already an electron on it then a possible second electron would be repulsed via the Coulomb interaction of magnitude U_H. This inter-orbital interaction makes it energetically costly to have a filling of two electrons on 1-orbital. Consequently, the occupation of the electrons shift among 2,3- and 1-orbitals until the occupation vector becomes $\vec{n} = (1, 1)^T$. Note that at $J = 0$ ($U = U_H$) nothing would stop the electrons to reach the filling of $\vec{n} = (2, 0)^T$, which shows the crucial role of the Hund's coupling for the crystal fields with negative splitting parameter $\Delta < 0$. At filling (1,1) the single-orbital is half-filled while the double-orbital is quarter-filled. Both can go through a Mott-transition at a certain critical interaction: the first one at U_c^1 and the other ones at U_c^{23}. If both the critical interaction values are smaller than the interaction which was needed to achieve the (1,1)-occupation $U_c^1, U_c^{23} < U_c^{occ}$ then all orbitals are insulating, see Fig. 13 (b). The symmetric aspect of the single-orbital spectral function is once again due to the half-filling, but the Hubbard bands are shifted because of the Hund's coupling among the orbitals. For the multi-orbital spectral functions, the quarter-filling means that 1/4 of the total spectral weight is on the left side and the rest is on the right side. On the other hand, for $U_c^1 < U_c^{occ} < U_c^{23}$ the Orbital Selective Mott Transition can be observed, see Fig. 14. Here, the single-orbital is already in its Mott insulating phase while the multi-orbitals are in their metallic phases. Since it is just a small regime where the OSMT occurs, it is difficult

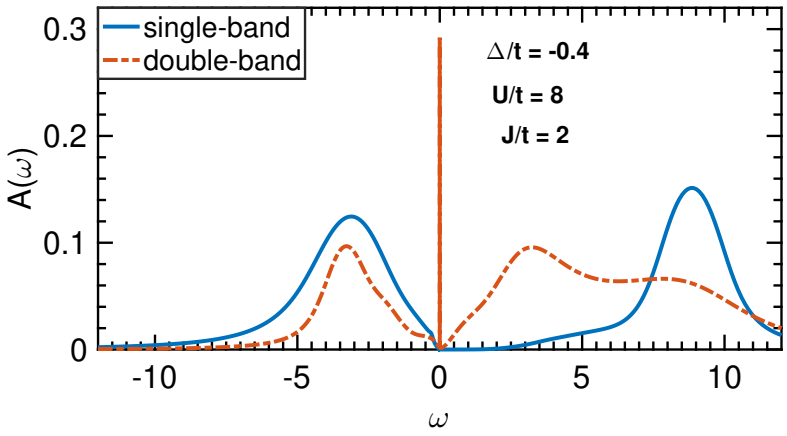

Figure 14: Spectral functions of the orbital-selective Mott phase for the crystal field with negative splitting parameter $\Delta/t = -0.4$, where the single-band is in a Mott insulating phase while the degenerate double bands are metallic.

to find a metallic phase for the double-band, for which the quasi-particle weight is larger, i.e. for which the peak at $\omega = 0$ is wider. Nevertheless the plotted spectral function have converged for the computations so we can confidently state that Fig. 14. is a legitimate OSMP. Concerning the phase diagram of the crystal fields with negative splitting parameter, the OSMT is always at the boarders of the hysteresis, creating a new layer in between the pure metallic and pure Mott insulating regimes. Out of all computations of this thesis, we needed the most accurate and also the most time-consuming NRG iterations for the OSM-phases. We realized that finding converged results for the OSMT could have been easier for a wider shifting of the orbitals. For instance if $\Delta/t \approx -1$ the $U-$interval for which the OSMT can be observed, is larger than for $\Delta/t = -0.4$. Consequently, the areas between the hysteresis and the pure phases are wider. Thus the OSM-phases are not so close to their critical interaction values and the convergence can be reached easier and faster. In Fig. 15 we can see how the regimes of the OSMP appear at the boarder of the hysteresis making two new layers between and the pure metallic and insulating phases.

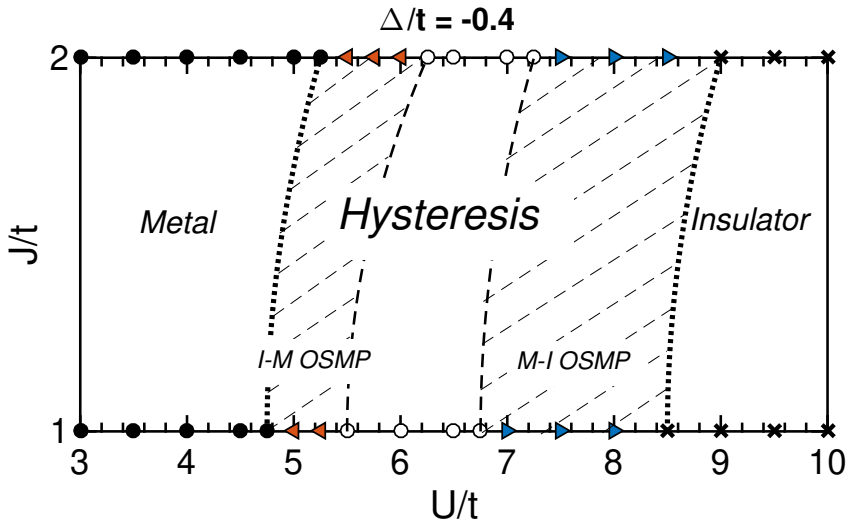

Figure 15: Phase diagram of the crystal field with negative splitting parameter $\Delta/t = -0.4$. Showing the different regimes on the $J-U-$plane, from left to right: metallic phases, OSMP for the insulator-metal transition, coexistent phases where for a metallic seed all bands are metallic and for an insulating seed all bands are insulating, OSMP for the metal-insulator transition and finally the Mott insulator phases. Computed phases are labelled with filled circles (metallic), orange triangles pointing to the left (I-M OSMP), hollow circles (coexistent), blue triangles pointing to the right (M-I OSMP) and crosses (Mott-insulating).

Each of the found orbital-selective phases (triangles in the figure) are like the ones we discussed earlier Fig. 14, i.e. phases where the double-bands are metallic and the single-band is Mott-insulating. This observation verifies our theoretical expectations, i.e. in the investigated crystal fields, the critical interaction of the double-bands U_c^{23} at quarter-filling is larger than the critical interaction of the single-band U_c^1 at half-filling. Let us interpret what happens with a metallic phase as the Coulomb interaction is increased. In the beginning all bands are metallic until the interaction reaches the M-I OSMP regime (around $U/t = 7$). At this point the single-band becomes Mott insulating because its critical value U_c is smaller than $U/t = 7$, but the double-band remains metallic. Increasing the interaction even more, turns the higher-lying double band also Mott insulating (around $U/t = 8.5$). An insulating seed goes through the same transitions but in the other direction and its I-M OSMP region lies at a smaller interaction U. (Note that the M-I OSMP region is only for the metallic - and the I-M OSMP region is only for the insulating initial hybridizations.) Contrary to our results, the width of the two OSMP regimes were expected to be equal, since theoretically they do not depend on the direction of the Mott transition (I-M or M-I). However if we take into account how difficult it is to reach convergence for the OSMT, the difference between the widths of the OSMP regimes can sign the possible deviations. Keeping in mind how large the deviation was for the (simpler) single-orbital Mott transition, we can estimate it to be around $U/t = \pm 1$ for the multi-orbital model. But

even considering the relatively large error we can see a general shift to the left for the critical interaction values and thus for the different regimes in comparison to the three-fold degenerate case Fig. 10. Just like for the positive splitting parameter, this is also verified by [62]. With our results we can formulate that the critical values U_c decrease for $|\Delta| \leq 0.4t$ and this tendency does not change until $|\Delta| \approx t$ [62].

4 Conclusion and Outlook

In this thesis, we introduced the single-orbital, the fully degenerate and via the crystal field splitting the semi-degenerate three-orbital Hubbard models for the strongly correlated electronic systems at $T = 0$. In each of the models we have investigated the Mott-Hubbard metal-insulator transitions and then for the multi-orbital cases we have mapped out the phase diagrams as a function of the Coulomb interaction U and the Hund's coupling J. In order to tell if the system went through the metal-insulator transition, we analysed the characteristic spectral functions of the bands. Since the correlated system depends on many parameters, there are a lot of possible ways to interpret the Mott transitions. In our context, for the single-band model we had a fixed half-filling on the atomic sites $\langle N \rangle = 1$, which enforced a particle-hole symmetry and thus the spectral functions became symmetric. Here, we have varied the strength of the screened Coulomb repulsion U to see for which critical values U_c does the Mott transition occur. We have found two different values U_{c1} and U_{c2} depending on the direction of the transition. Between these boarders there is a coexistence regime called the hysteresis. For the multi-orbital models we fixed the total electron occupation to be $\langle N \rangle = 2$, for which the particle excitations are prevailing in comparison to the hole excitations. Since the electrons follow the Hund's rule as they fill up the bands, we implemented the Hund's coupling term J in the Hamiltonian, to ensure the incorporation of the filling-rules. J has significant effects on the system: 1) for $J = 0 \rightarrow J = 1$ it leads to smaller U_c and 2) for $J = 1 \rightarrow J > 1$ to larger critical interaction values U_c at filling $\langle N \rangle = 2$. The orbital-decoupling role of the Hund's term is also crucial for the crystal fields, since it affects the redistribution of the electrons on the site while increasing the Coulomb interaction. We have examined the simplest version of the three-orbital crystal fields, where the energy levels of the separate single-band and of the two degenerate bands have been shifted apart with the fixed splitting parameter $\Delta/t = +0.4$ and $\Delta/t = -0.4$. Depending on the sign of Δ, different outcomes are possible. The negative splitting parameter induced a type of phase, the orbital-selective Mott phase, which was not present for any of the previous models. In this phase the single-band was Mott-insulating while the double-band was still metallic. That is, in this interesting phenomena part of the electrons are localized and thus not conducting while the other part is fully de-localized and itinerant.

In order to find quantitative results for the characteristic spectral functions of the system, we treated the Hubbard models in the framework of the Dynamical Mean-Field Theory (DMFT). This theory maps the (lattice) Hubbard model onto a self-consistent quantum impurity model and thus it reduces the many-body system to a single-site (impurity) problem with effective and local parameters. In the limit of infinite dimensions the DMFT calculations lead to exact results for the hybridization function, which are closely connected to the spectral functions on a Bethe lattice. From an input hybridization we can determine the eigenenergies of the Hamiltonian and consequently the local self-energy iteratively. We used a DMFT+NRG code provided by the group of Jan von Delft. The NRG method due to its logarithmic scaling of the energy spectrum ensures a high resolution around the Fermi energy, which is undoubtedly the most important energy regime for the Mott transitions. An important aspect of the NRG method is the possible truncation of the set of eigenstates (due to the exponential decay of the hopping matrix elements among the sites) during the iterative diagonalization of the Hamiltonian (Wilson chain). This procedure keeps a fixed amount of low-energy states after every iteration step, which fixes the size of the Hilbert space and thus makes the computations numerically tractable. Although the high-energy states do not influence the physics of the low-energy states significantly, one has to be careful with discarding too many states because it can still affect the outcome. An arbitrary artefact in the NRG calculations can increase in each of the DMFT iteration loops and thus it can lead to a large deviation. Concerning the deviations, our results could have been more accurate by taking enhanced NRG parameters, but this would have been much more time-consuming. Nevertheless, we tried to improve the accuracy around the Mott transition (where the convergence is more difficult to achieve) by increasing the number of kept states and by making the logarithmic discretization finer (by lowering Λ). Despite these possible sources of error, we were able to reproduce the MIT for the different Hubbard models and plot their spectral functions on the real frequency axis. Although our results are more qualitative than quantitative, we could still get a general idea how the Hubbard interaction, Hund's coupling and crystal field splitting affect the strongly correlated systems. Note that there is no universal way to treat correlated materials. We used the DMFT+NRG method, but there is also the Quantum

Monte Carlo (QMC) [53] and Many-Body Perturbation Theory [63] methods. Each of them has their strengths and weaknesses and each of them are relevant even today, discussed in [64].
While investigating the crystal fields, we have realized that different physics could be present for a stronger Δ/t [62]. Our results with the relatively small splitting parameters could serve as a basis for the future computations of the crystal fields with $|\Delta/t| \gtrsim 1$. However, this is just one of the many options we could use the DMFT+NRG method for. A possible extension to our calculations would be to implement the spin-orbit coupling, i.e. to incorporate the third Hund's rule which could lead to new physical effects. Also, we always assumed a diagonal kinetic matrix, but maybe considering hoppings among the different orbitals on the same site and not just among the neighbouring sites, would reflect the reality even better. It would be interesting to see the influence of the non-diagonal hopping together with the crystal field splitting on the Mott transition. Another possibility for the future would be to examine the effect of finite temperatures on the spectral functions [24]. This extension would lead to new combinations of fixed and varied parameters of $\langle N \rangle, U, J, \Delta, T$.

Appendices

Appendix A Lattice Fermions in Infinite Dimensions

Since it is not trivial to take the limit of infinite dimensions of the Hubbard model with itinerant quantum-mechanical degrees of freedom, let us explain it in this appendix using the thought process of [14]. Both the interaction and the chemical potentials are purely local and thus independent of the lattice structure and dimensions, i.e. we only need to investigate how the kinetic term behaves in this limit. Following [4], we will consider a simple $d-$ dimensional hypercubic lattice with the dispersion

$$\varepsilon_{\mathbf{k}} = -2t \sum_{i=1}^{d} \cos \mathbf{k}_i \,. \tag{A.1}$$

where the coordination number $Z = 2d$ and $\hbar, k_B := 1$. With the dispersion relation we can write up the density of states as

$$N_d(\omega) = \sum_{\mathbf{k}} \delta(\omega - \varepsilon_{\mathbf{k}}) \,. \tag{A.2}$$

That is, N_d is the probability density for finding $\omega = \varepsilon_{\mathbf{k}}$ for any $\mathbf{k} = (k_1, .., k_d)$. Since the central limit theorem states that the sum of independent and identically distributed random variables with finite variances will tend to a normal distribution as the number of variables increases, we can assume the density of states to have a form of a Gaussian. The next step is to take the infinite dimensions limit of (A.2) while using the central limit theorem,

$$N_d(\omega) \overset{d\to\infty}{\longrightarrow} \frac{1}{2t\sqrt{\pi d}} \exp\left[-\left(\frac{\omega}{2t\sqrt{d}} \right)^2 \right] . \tag{A.3}$$

As we can see, this Gaussian peak becomes arbitrarily broad for $d \to \infty$ which would lead to incorrect density of states for the particles in the solid. In order to overcome this problem, one needs to scale the kinetic term t properly. Only the following hopping amplitude scaling yields a non-trivial DOS

$$t \to \frac{t^*}{\sqrt{Z}} \,,\; t^* = \text{const.} \quad \Rightarrow \quad N_{d=\infty}(\omega) = \frac{1}{\sqrt{2\pi} t^*} \exp\left[-\frac{1}{2} \left(\frac{\omega}{t^*} \right)^2 \right] , \tag{A.4}$$

which leads to the Hamiltonian

$$H = -\mu \sum_{i\sigma} n_{i\sigma} - \frac{t^*}{\sqrt{Z}} \sum_{\langle i,j \rangle \sigma} c^\dagger_{i\sigma} c_{j\sigma} + U \sum_i n_{i\uparrow} n_{i\downarrow} \,. \tag{A.5}$$

This Hubbard Hamiltonian has a non-trivial $Z \to \infty$ limit, where the magnitude of the kinetic and interaction terms remain comparable, therefore the competition between them is still possible. Thus we showed that with the scaling the physics of the system is still retained. The purpose of taking the limit of infinite dimensions is to simplify the calculations of the Hubbard lattice model significantly. The kinetic term can be written as

$$E_{kin} = \frac{t^*}{\sqrt{z}} \sum_{\langle ij \rangle} \langle c^\dagger_{i\sigma} c_{j\sigma} \rangle = \lim_{t \to 0^+} \frac{t^*}{\sqrt{z}} \sum_{\langle ij \rangle} \int_{-\infty}^{\infty} \frac{d\omega}{2\pi i} G_{ij}(\omega) e^{i\omega t} \,. \tag{A.6}$$

For general i, j the one-particle and time-ordered Green's function $G_{ij\sigma}(\omega)$ scales as [65]

$$G_{ij\sigma} \sim \mathcal{O}(1/d^{\|\boldsymbol{R}_i - \boldsymbol{R}_j\|/2}) \,, \tag{A.7}$$

where $\|\boldsymbol{R}\| = \sum_{n=1}^{d} |R_n|$ is the length of $\boldsymbol{R}$ in the 'Manhattan metric'. This property leads to the collapse of all connected, irreducible perturbation theory diagrams in position space [4].

Consequently, the full, irreducible self-energy becomes a purely local quantity

$$\Sigma_{ij\sigma}(\omega) \overset{d\to\infty}{=} \Sigma_{ii\sigma}(\omega)\delta_{ij}\,. \tag{A.8}$$

The Fourier transform of the self-energy preserves this property as well

$$\Sigma_{\sigma}(\boldsymbol{k},\omega) \overset{d\to\infty}{\equiv} \Sigma_{\sigma}(\omega)\,. \tag{A.9}$$

Appendix B Equation of Motion in Quantum Many-Particle Theory

The following appendices are based on the ones from K. Stadler's master thesis [18]. Here we will derive the form of the equation of motion in the quantum many-particle systems, which will be used in the following appendices to derive the lattice and impurity Green's function, i.e. the key DMFT equations. Let us first define the retarded Green's function as

$$G_{AB}(t) = \langle\langle A; B\rangle\rangle_t \equiv -i\Theta(t)\langle\{A(t), B(0)\}\rangle_T \,, \tag{B.1}$$

with the fermionic operators A, B and the subscription of $\langle\,\cdot\,\rangle_T$ denotes that it is the thermal average in the grand canonical ensemble, i.e. $\langle\{A(t), B(0)\}\rangle_T = \operatorname{Tr}\rho\{A, B\}$. In the Heisenberg picture the time development of the operators can be written as $A(t) = e^{iHt}Ae^{-iHt}$. Accordingly, the equation of motion of the operator A in the Heisenberg picture is

$$\frac{d}{dt}A(t) = \frac{i}{\hbar}[H, A](t) \,. \tag{B.2}$$

Using (B.2) for both operators A, B in (B.1), we can derive the equation of motion for the Green's function

$$\begin{aligned} \frac{d}{dt}G_{AB}(t) &= -i\delta(t)\langle\{A(0), B(0)\}\rangle_T - i\Theta(t)\langle\{i[H, A](t), B(0)\}\rangle_T \\ &= -i\delta(t)\langle\{A(0), B(0)\}\rangle_T - i\langle\langle[A, H](t); B(0)\rangle\rangle_t \,. \end{aligned} \tag{B.3}$$

A Fourier transformation yields the equation of motion in frequency space,

$$\omega\langle\langle A; B\rangle\rangle_\omega = \langle\{A, B\}\rangle_T + \langle\langle[A, H]; B\rangle\rangle_\omega \,, \tag{B.4}$$

with

$$\langle\langle A; B\rangle\rangle_\omega = \int_{-\infty}^{\infty} dt\, \langle\langle A; B\rangle\rangle_t\, e^{i\omega t} \,.$$

The spectral function is defined in time space as

$$A_{AB}(t) = \frac{1}{2\pi}\langle\{A(t), B(0)\}\rangle_T \quad \Rightarrow \quad \langle\{A(t), B(0)\}\rangle_T = 2\pi A_{AB}(t) \,. \tag{B.5}$$

Let us derive the equivalent definition of the spectral function in frequency space using the Fourier transformation and a particular notation of the Heaviside step function $\Theta(t)$ (*)

$$\begin{aligned} G_{AB}(\omega) &\overset{B.1}{\underset{B.5}{=}} \int_{-\infty}^{\infty} dt\, e^{i\omega t}\big(-i\Theta(t)2\pi A_{AB}(t)\big) \\ &= \int_{-\infty}^{\infty} dt\, e^{i\omega t}(-i\Theta(t)) \int_{-\infty}^{\infty} d\omega'\, A_{AB}(\omega')e^{-i\omega' t} \\ &\overset{(*)}{=} \int_{-\infty}^{\infty} d\omega' \int_{-\infty}^{\infty} dx\, \frac{A_{AB}(\omega')}{x + i0^+} \cdot \frac{1}{2\pi}\int_{-\infty}^{\infty} dt\, e^{-i(x-(\omega-\omega')t)} \\ &= \int_{-\infty}^{\infty} d\omega' \int_{-\infty}^{\infty} dx\, \frac{A_{AB}(\omega')}{x + i0^+}\delta\big(x - (\omega - \omega')\big) \\ &= \int_{-\infty}^{\infty} d\omega'\, \frac{A_{AB}(\omega')}{\omega - \omega' + i0^+} \,, \end{aligned} \tag{B.6}$$

where the last term is also called as the spectral representation of the (retarded) Green's function. Note that $i0^+$ ensures that the Green's function is analytical in the upper half plane. Using the Sokhotski-Plemelj theorem (**)

$$\frac{1}{\omega - \omega' + i0^+} = \mathcal{P}\frac{1}{\omega - \omega'} - i\pi\delta(\omega - \omega') \,,$$

where $\mathcal{P}$ is the Cauchy principle value of the function $1/x$. Inserting (**) in (B.6), we can derive the desired definition of the spectral function in frequency space

$$A_{AB}(\omega) = -\frac{1}{\pi} \operatorname{Im} G_{AB}(\omega)\,. \tag{B.7}$$

Appendix C Lattice Green's Function in the Multi-Band Model

After determining the local self-energy from an input hybridization using NRG, the next step in the DMFT iteration loop is to calculate the lattice Green's function. Thus it is necessary to derive the lattice Green's function $G^{\nu\eta}_{latt,\mathbf{k}}(\omega) = \langle\langle c_{\mathbf{k}\eta}; c^\dagger_{\mathbf{k}\nu}\rangle\rangle_\omega$ of a system described by the Hamiltonian

$$\begin{aligned} H &= \sum_{\mathbf{k}\bar{\eta}\bar{\nu}} \varepsilon^{\bar{\eta}\bar{\nu}}_{\mathbf{k}} c^\dagger_{\mathbf{k}\bar{\eta}} c_{\mathbf{k}\bar{\nu}} - \sum_{\mathbf{k}\bar{\eta}} \mu_{\bar{\eta}} c^\dagger_{\mathbf{k}\bar{\eta}} c_{\mathbf{k}\bar{\eta}} + \sum_i H^{loc}_{int} \\ &= H^0 + H^{loc}_{int}\,, \end{aligned} \tag{C.1}$$

with the non-interacting H^0 and the local interaction term H^{loc}_{int} in the spatial representation. $\eta = \{m\sigma\}$ and $\nu = \{m'\sigma'\}$ label the different orbital $m = 1, 2, ..., M$ and spin $\sigma = \uparrow, \downarrow$ indices. We use the equation of motion (B.3) for the non-interacting lattice Green's function $G^{0,\eta\nu}_{latt,\mathbf{k}} = \langle\langle c_{\mathbf{k}\eta}; c^\dagger_{\mathbf{k}\nu}\rangle\rangle^0_t$

$$i\frac{d}{dt}\langle\langle c_{\mathbf{k}\eta}; c^\dagger_{\mathbf{k}\nu}\rangle\rangle^0_t = \delta(t)\langle\{c_{\mathbf{k}\eta}, c^\dagger_{\mathbf{k}\nu}\}\rangle_T + \langle\langle [H^0, c_{\mathbf{k}\eta}]; c^\dagger_{\mathbf{k}\nu}\rangle\rangle_t\,. \tag{C.2}$$

Using the anti-commutation relation $\{c_{\mathbf{k}\eta}, c^\dagger_{\mathbf{k}\nu}\} = \delta_{\eta\nu}$ and commutation relations for

$$[H^0, c_{\mathbf{k}\eta}] = \sum_{\bar{\mathbf{k}}\bar{\eta}} \underbrace{[c^\dagger_{\bar{\mathbf{k}}\bar{\eta}} c_{\bar{\mathbf{k}}\bar{\eta}}, c_{\mathbf{k}\eta}]}_{-\delta_{\bar{\eta}\eta}\delta_{\bar{\mathbf{k}}\mathbf{k}} c_{\bar{\mathbf{k}}\bar{\eta}}} + \sum_{\bar{\mathbf{k}}\bar{\eta}\bar{\nu}} \varepsilon^{\bar{\eta}\bar{\nu}}_{\bar{\mathbf{k}}} \underbrace{[c^\dagger_{\bar{\mathbf{k}}\bar{\eta}} c_{\mathbf{k}\bar{\nu}}, c_{\mathbf{k}\eta}]}_{-\delta_{\bar{\eta}\eta}\delta_{\bar{\mathbf{k}}\mathbf{k}} c_{\bar{\mathbf{k}}\bar{\nu}}}$$

results in

$$i\frac{d}{dt}\langle\langle c_{\mathbf{k}\eta}; c^\dagger_{\mathbf{k}\nu}\rangle\rangle^0_t = \delta(t)\delta_{\eta\nu} - \mu_\eta\langle\langle c_{\mathbf{k}\eta}; c^\dagger_{\mathbf{k}\nu}\rangle\rangle^0_t + \sum_{\bar{\nu}} \varepsilon^{\eta\bar{\nu}}_{\mathbf{k}}\langle\langle c_{\mathbf{k}\bar{\nu}}; c^\dagger_{\mathbf{k}\nu}\rangle\rangle^0_t\,. \tag{C.3}$$

The last term can be written in a more compact way as

$$\sum_{\bar{\nu}} \left[(i\frac{d}{dt} + \mu_\eta)\delta_{\eta\bar{\nu}} - \varepsilon^{\eta\bar{\nu}}_{\mathbf{k}}\right]\langle\langle c_{\mathbf{k}\bar{\nu}}; c^\dagger_{\mathbf{k}\nu}\rangle\rangle^0_t = \delta(t)\delta_{\eta\nu}\,. \tag{C.4}$$

The Fourier transformation leads to

$$\sum_{\bar{\nu}} \left[(\omega + \mu_\eta)\delta_{\eta\bar{\nu}} - \varepsilon^{\eta\bar{\nu}}_{\mathbf{k}}\right]\langle\langle c_{\mathbf{k}\bar{\nu}}; c^\dagger_{\mathbf{k}\nu}\rangle\rangle^0_\omega = \delta_{\eta\nu}\,, \tag{C.5}$$

which written in matrix notations gives

$$\left[(\omega + \mu)\mathbb{1} - \varepsilon_{\mathbf{k}}\right]G^0_{latt,\mathbf{k}}(\omega) = \mathbb{1}\,. \tag{C.6}$$

Accordingly, the inverse of the non-interacting Green's function reads

$$G^0_{latt,\mathbf{k}}(\omega)^{-1} = (\omega + \mu)\mathbb{1} - \varepsilon_{\mathbf{k}}\,. \tag{C.7}$$

The next step is to use the Dyson equation, which connects the non-interacting and interacting Green's function of the lattice via the self-energy $\Sigma(\omega)$

$$G_{latt,\mathbf{k}}(\omega)^{-1} = G^0_{latt,\mathbf{k}}(\omega)^{-1} - \Sigma(\omega) = (\omega + \mu)\mathbb{1} - \varepsilon_{\mathbf{k}} - \Sigma(\omega)\,. \tag{C.8}$$

Finally, the lattice Green's function yields

$$G^{m\sigma,m'\sigma'}_{latt,\mathbf{k}}(\omega)^{-1} = \langle\langle c_{\mathbf{k}m\sigma}; c^\dagger_{\mathbf{k}m'\sigma'}\rangle\rangle^{-1}_\omega = \delta_{\sigma\sigma'}\left[(\omega + \mu_m)\delta_{mm'} - \varepsilon^{mm'}_{\mathbf{k}} - \Sigma_{mm'}(\omega)\right]. \tag{C.9}$$

For the single-orbital Hubbard model (with skipped spin and orbital indices) the last expression reduces to

$$G_{latt,\mathbf{k}} = \frac{1}{\omega + \mu + -\varepsilon_{\mathbf{k}} - \Sigma(\omega)}\,. \tag{C.10}$$

Appendix D Impurity Green's Function and Self-Energy

From the lattice Green's function, we can derive the impurity Green's function and using the self-consistency condition we can find an expression for the local self-energy of the Single-Impurity Anderson Model (SIAM), which will serve as the new input hybridization for the next iteration step. Accordingly, we use the SIAM Hamiltonian from (2.1.19)

$$H_{SIAM} = H_{imp} + H_{bath} + H_{hyb}\,, \tag{D.1}$$

$$H_{imp} = \sum_{\bar{\eta}} \varepsilon_d^{\bar{\eta}} d_{\bar{\eta}}^\dagger d_{\bar{\eta}} + H_{int}^{loc}\,, \tag{D.2}$$

$$H_{bath} = \sum_{k\in 1.BZ} \sum_{\bar{\nu}} \varepsilon_k^{\bar{\nu}} c_{k\bar{\nu}}^\dagger c_{k\bar{\nu}}\,, \tag{D.3}$$

$$H_{hyb} = \sum_{k\in 1.BZ} \sum_{\bar{\eta}\bar{\nu}} V_k^{\bar{\eta}\bar{\nu}} (d_{\bar{\eta}}^\dagger c_{k\bar{\nu}} + c_{k\bar{\nu}}^\dagger d_{\bar{\eta}})\,, \tag{D.4}$$

but with the general quantum numbers $\eta = \{m\sigma\}, \nu = \{m'\sigma'\}$, where $m = 1, 2, ..., M$ is the orbital and $\sigma = \uparrow, \downarrow$ is the spin index of the quantities. H_{int}^{loc} denotes an arbitrary local interaction term on the impurity site, which in the case of a strongly correlated electronic system would be a Coulomb repulsion. Similar to the lattice Green's function, the retarded impurity Green's function is given by $G^{\eta\nu}(\omega) = \langle\langle d_\eta; d_\nu^\dagger\rangle\rangle_\omega$ and the equation of motion as

$$\omega\langle\langle d_\eta; d_\nu^\dagger\rangle\rangle_\omega = \langle\{d_\eta, d_\nu^\dagger\}\rangle_T - \langle\langle [H, d_\eta]; d_\nu^\dagger\rangle\rangle_\omega\,. \tag{D.5}$$

In order to calculate the RHS of the equation of motion, we need to use the anti-commutation $\{d_\eta, d_\nu^\dagger\} = \delta_{\eta\nu}$ and the commutation relations for

$$[H_{SIAM}, d_\eta] = \sum_{\bar{\eta}} \varepsilon_d^{\bar{\eta}} \underbrace{[d_{\bar{\eta}}^\dagger d_{\bar{\eta}}, d_\eta]}_{-\delta_{\bar{\eta}\eta} d_{\bar{\eta}}} + [H_{int}^{loc}, d_\eta] \tag{D.6}$$

$$+ \sum_{k\in 1.BZ} \sum_{\bar{\nu}} \varepsilon_k^{\bar{\nu}} \underbrace{[c_{k\bar{\nu}}^\dagger c_{k\bar{\nu}}, d_\eta]}_{0} \tag{D.7}$$

$$+ \sum_{k\in 1.BZ} \sum_{\bar{\eta}\bar{\nu}} V_k^{\bar{\eta}\bar{\nu}} (\underbrace{[d_{\bar{\eta}}^\dagger c_{k\bar{\nu}}, d_\eta]}_{-\delta_{\bar{\eta}\eta} c_{k\bar{\nu}}} + \underbrace{[c_{k\bar{\nu}}^\dagger d_{\bar{\eta}}, d_\eta]}_{0})\,. \tag{D.8}$$

Inserting it back into the equation of motion gives

$$\omega\langle\langle d_\eta; d_\nu^\dagger\rangle\rangle_\omega = \delta_{\eta\nu} + \varepsilon_d^\eta \langle\langle d_\eta; d_\nu^\dagger\rangle\rangle_\omega + \langle\langle [d_\eta, H_{int}^{loc}]; d_\nu^\dagger\rangle\rangle_\omega + \sum_{k\in 1.BZ} \sum_{\bar{\eta}\bar{\nu}} V_k^{\bar{\eta}\bar{\nu}} \langle\langle c_{k\bar{\nu}}; d_\nu^\dagger\rangle\rangle_\omega\,, \tag{D.9}$$

where the last term is not in a desired form, since it has bath fermionic operators $c_{k\bar{\nu}}$. It is possible to express $\langle\langle c_{k\bar{\nu}}; d_\nu^\dagger\rangle\rangle_\omega$ in terms of the impurity correlation $\langle\langle d_\eta; d_\nu^\dagger\rangle\rangle_\omega$ via the equation of motion

$$\omega\langle\langle c_{k'\nu'}; d_\nu^\dagger\rangle\rangle_\omega = \langle\{c_{k'\nu'}, d_\nu^\dagger\}\rangle_T - \langle\langle [H_{SIAM}, c_{k'\nu'}]; d_\nu^\dagger\rangle\rangle_\omega\,, \tag{D.10}$$

with

$$\{c_{k'\nu'}, d_\nu^\dagger\} = 0 \tag{D.11}$$

$$[H_{SIAM}, c_{k'\nu'}] = \sum_{\bar{\eta}} \varepsilon_d^{\bar{\eta}} \underbrace{[d_{\bar{\eta}}^\dagger d_{\bar{\eta}}, c_{k'\nu'}]}_{0} + \underbrace{[H_{int}^{loc}, c_{k'\nu'}]}_{0} \tag{D.12}$$

$$+ \sum_{k\in 1.BZ} \sum_{\bar{\nu}} \varepsilon_k^{\bar{\nu}} \underbrace{[c_{k\bar{\nu}}^\dagger c_{k\bar{\nu}}, c_{k'\nu'}]}_{-\delta_{k\bar{k}}\delta_{\bar{\nu}\nu'} c_{k\bar{\nu}}} \tag{D.13}$$

$$+ \sum_{k\in 1.BZ} \sum_{\bar{\eta}\bar{\nu}} V_k^{\bar{\eta}\bar{\nu}} (\underbrace{[d_{\bar{\eta}}^\dagger c_{k\bar{\nu}}, c_{k'\nu'}]}_{0} + \underbrace{[c_{k\bar{\nu}}^\dagger d_{\bar{\eta}}, c_{k'\nu'}]}_{-\delta_{k\bar{k}}\delta_{\bar{\nu}\nu'} d_{\bar{\eta}}})\,, \tag{D.14}$$

we get

$$\omega\langle\langle c_{k'\nu'}; d_\nu^\dagger\rangle\rangle_\omega = \varepsilon_{k'}^{\nu'}\langle\langle c_{k'\nu'}; d_\nu^\dagger\rangle\rangle_\omega + \sum_{\bar{\eta}} V_k^{\bar{\eta}\nu'}\langle\langle d_{\bar{\eta}}; d_\nu^\dagger\rangle\rangle_\omega \tag{D.15}$$

and finally

$$\langle\langle c_{k'\nu'}; d_\nu^\dagger\rangle\rangle_\omega = \frac{\sum_{\bar{\eta}} V_{k'}^{\bar{\eta}\nu'}\langle\langle d_{\bar{\eta}}; d_\nu^\dagger\rangle\rangle_\omega}{\omega - \varepsilon_{k'}^{\nu'}}\,. \tag{D.16}$$

Consequently, the original equation of motion (D.9) reads

$$\omega\langle\langle d_\eta; d_\nu^\dagger\rangle\rangle_\omega = \delta_{\eta\nu} + \varepsilon_d^\eta\langle\langle d_\eta; d_\nu^\dagger\rangle\rangle_\omega + \underbrace{\langle\langle [d_\eta, H_{int}^{loc}]; d_\nu^\dagger\rangle\rangle_\omega}_{=:F_{\eta\nu}(\omega)} + \sum_{\bar{\eta}} \underbrace{\sum_{k\bar{\nu}} \frac{V_k^{\eta\bar{\nu}} V_k^{\bar{\eta}\bar{\nu}}}{\omega - \varepsilon_k^{\bar{\nu}}}}_{=:\Delta_{\eta\bar{\eta}}(\omega)} \langle\langle d_{\bar{\eta}}; d_\nu^\dagger\rangle\rangle_\omega\,, \tag{D.17}$$

which can be written as

$$\sum_{\bar{\eta}} [(\omega - \varepsilon_d^\eta)\delta_{\eta\bar{\eta}} - \Delta_{\eta\bar{\eta}}(\omega)]\langle\langle d_{\bar{\eta}}; d_\nu^\dagger\rangle\rangle_\omega - F_{\eta\nu}(\omega) = \delta_{\eta\nu}\,, \tag{D.18}$$

and in matrix notation

$$[(\omega - \varepsilon_d)\mathbb{1} - \Delta(\omega)]G(\omega) - F(\omega) = \mathbb{1}\,. \tag{D.19}$$

The impurity Green's function yields

$$G(\omega)^{-1} = (\omega - \varepsilon_d)\mathbb{1} - \Delta(\omega) - \Sigma(\omega) \quad \text{with} \quad \Sigma(\omega) = F(\omega)G(\omega)^{-1}\,. \tag{D.20}$$

For the single band case (with skipped spin and orbital indices) this expression simplifies to

$$G_{imp}(\omega) = \langle\langle d; d^\dagger\rangle\rangle_\omega = \frac{1}{\omega - \varepsilon_d - \Delta(\omega) - \Sigma(\omega)}\,, \quad \text{with} \quad \Delta(\omega) = \sum_k \frac{V_k^2}{\omega - \varepsilon_k}\,. \tag{D.21}$$

Last but not least, the self-energy trick used in the NRG computations [21] is also derived as

$$\Sigma(\omega) = \frac{F(\omega)}{G_{imp}(\omega)}\,. \tag{D.22}$$

References

[1] J. Hubbard. Electron correlations in narrow energy bands. *Proceedings of the Royal Society of London A: Mathematical, Physical and Engineering Sciences*, 276(1365):238–257, 1963.

[2] Martin C. Gutzwiller. Effect of correlation on the ferromagnetism of transition metals. *Phys. Rev. Lett.*, 10:159–162, Mar 1963.

[3] Junjiro Kanamori. Electron correlation and ferromagnetism of transition metals. *Progress of Theoretical Physics*, 30(3):275–289, 1963.

[4] Walter Metzner and Dieter Vollhardt. Correlated lattice fermions in $d = \infty$ dimensions. *Phys. Rev. Lett.*, 62:324–327, Jan 1989.

[5] Antoine Georges and Gabriel Kotliar. Hubbard model in infinite dimensions. *Phys. Rev. B*, 45:6479–6483, Mar 1992.

[6] Antoine Georges, Gabriel Kotliar, Werner Krauth, and Marcelo J. Rozenberg. Dynamical mean-field theory of strongly correlated fermion systems and the limit of infinite dimensions. *Rev. Mod. Phys.*, 68:13–125, Jan 1996.

[7] J. E. Hirsch and R. M. Fye. Monte carlo method for magnetic impurities in metals. *Phys. Rev. Lett.*, 56:2521–2524, Jun 1986.

[8] G. Kotliar, S. Y. Savrasov, K. Haule, V. S. Oudovenko, O. Parcollet, and C. A. Marianetti. Electronic structure calculations with dynamical mean-field theory. *Rev. Mod. Phys.*, 78:865–951, Aug 2006.

[9] S. A. Jafari. Introduction to hubbard model and exact diagonalization. *Iranian J.Phys.Res.*, No.2, 2008.

[10] Kenneth G. Wilson. The renormalization group: Critical phenomena and the kondo problem. *Rev. Mod. Phys.*, 47:773–840, Oct 1975.

[11] H. R. Krishna-murthy, J. W. Wilkins, and K. G. Wilson. Renormalization-group approach to the anderson model of dilute magnetic alloys. ii. static properties for the asymmetric case. *Phys. Rev. B*, 21:1044–1083, Feb 1980.

[12] Ralf Bulla, Theo A. Costi, and Thomas Pruschke. Numerical renormalization group method for quantum impurity systems. *Rev. Mod. Phys.*, 80:395–450, Apr 2008.

[13] P. W. Anderson. Localized magnetic states in metals. *Phys. Rev.*, 124:41–53, Oct 1961.

[14] Dieter Vollhardt Eva Pavarini, Erik Koch and Alexander Lichtenstein. The lda+dmft approach to strongly correlated materials. *Lecture notes of the Autumn School 2011.*

[15] Introduction to green functions and many-body perturbation theory, `http://folk.ntnu.no/johnof/green-2013.pdf`.

[16] Henrik Bruus Karsten and Flensberg. *Introduction to Many-body quantum theory in condensed matter physics.* 2002.

[17] Martin Eckstein, Marcus Kollar, Krzysztof Byczuk, and Dieter Vollhardt. Hopping on the bethe lattice: Exact results for densities of states and dynamical mean-field theory. *Phys. Rev. B*, 71:235119, Jun 2005.

[18] Katharina Maria Stadler. Towards exploiting non-abelian symmetries in the dynamical mean-field theory using the numerical renormalization group. Master's thesis, Ludiwg-Maximilians-Universität München, 2013.

[19] Osamu Sakai, Yukihiro Shimizu, and Tadao Kasuya. Single-particle and magnetic excitation spectra of degenerate anderson model with finite f–f coulomb interaction. *Journal of the Physical Society of Japan*, 58(10):3666–3678, 1989.

[20] T. A. Costi, A. C. Hewson, and V. Zlatic. Transport coefficients of the Anderson model via the numerical renormalization group. *Journal of Physics Condensed Matter*, 6:2519–2558, March 1994.

[21] R Bulla, A C Hewson, and Th Pruschke. Numerical renormalization group calculations for the self-energy of the impurity anderson model. *Journal of Physics: Condensed Matter*, 10(37):8365, 1998.

[22] R. Bulla. Zero temperature metal-insulator transition in the infinite-dimensional hubbard model. *Phys. Rev. Lett.*, 83:136–139, Jul 1999.

[23] H. R. Krishna-murthy, J. W. Wilkins, and K. G. Wilson. Renormalization-group approach to the anderson model of dilute magnetic alloys. i. static properties for the symmetric case. *Phys. Rev. B*, 21:1003–1043, Feb 1980.

[24] R. Bulla, T. A. Costi, and D. Vollhardt. Finite-temperature numerical renormalization group study of the mott transition. *Phys. Rev. B*, 64:045103, Jun 2001.

[25] C. Lanczos. An iteration method for the solution of the eigenvalue problem of linear differential and integral operators. *J. Res. Nat'l Bur. Std. 45*, 1950.

[26] H. R. Krishna-murthy, J. W. Wilkins, and K. G. Wilson. Renormalization-group approach to the anderson model of dilute magnetic alloys. i. static properties for the symmetric case. *Phys. Rev. B*, 21:1003–1043, Feb 1980.

[27] H. R. Krishna-murthy, J. W. Wilkins, and K. G. Wilson. Renormalization-group approach to the anderson model of dilute magnetic alloys. ii. static properties for the asymmetric case. *Phys. Rev. B*, 21:1044–1083, Feb 1980.

[28] K. M. Stadler, A. K. Mitchell, J. von Delft, and A. Weichselbaum. Interleaved numerical renormalization group as an efficient multiband impurity solver. *Phys. Rev. B*, 93:235101, Jun 2016.

[29] Rok Žitko. Adaptive logarithmic discretization for numerical renormalization group methods. 180:1271–1276, 08 2009.

[30] Žiga Osolin and Rok Žitko. Padé approximant approach for obtaining finite-temperature spectral functions of quantum impurity models using the numerical renormalization group technique. *Phys. Rev. B*, 87:245135, Jun 2013.

[31] J. C. Slater and G. F. Koster. Simplified lcao method for the periodic potential problem. *Phys. Rev.*, 94:1498–1524, Jun 1954.

[32] D. Vollhardt, K. Byczuk, and M. Kollar. *Dynamical Mean-Field Theory*, page 203. 2012.

[33] Shiro Sakai. Theoretical study of multi-orbital correlated electron systems with hund's coupling. Master's thesis, University of Tokyo, 2006.

[34] Antoine Georges, Luca de' Medici, and Jernej Mravlje. Strong correlations from hund's coupling. *Annual Review of Condensed Matter Physics*, 4(1):137–178, 2013.

[35] T. Pruschke and R. Bulla. Hund's coupling and the metal-insulator transition in the two-band hubbard model. *European Physical Journal B*, 44:217–224, March 2005.

[36] Marcelo J. Rozenberg. Integer-filling metal-insulator transitions in the degenerate hubbard model. *Phys. Rev. B*, 55:R4855–R4858, Feb 1997.

[37] Th. Pruschke, D. L. Cox, and M. Jarrell. Hubbard model at infinite dimensions: Thermodynamic and transport properties. *Phys. Rev. B*, 47:3553–3565, Feb 1993.

[38] A. Koga, N. Kawakami, T. M. Rice, and M. Sigrist. Mott transitions in the multi-orbital systems. *Physica B Condensed Matter*, 359:1366–1368, April 2005.

[39] S. Florens, A. Georges, G. Kotliar, and O. Parcollet. Mott transition at large orbital degeneracy: Dynamical mean-field theory. *Phys. Rev. B*, 66:205102, Nov 2002.

[40] Erik Koch, Olle Gunnarsson, and Richard M. Martin. Filling dependence of the mott transition in the degenerate hubbard model. *Phys. Rev. B*, 60:15714–15720, Dec 1999.

[41] Philipp Werner, Emanuel Gull, and Andrew J. Millis. Metal-insulator phase diagram and orbital selectivity in three-orbital models with rotationally invariant hund coupling. *Phys. Rev. B*, 79:115119, Mar 2009.

[42] Ryszard Radwanski and Z Ropka. Strongly correlated crystal-field approach to mott insulator lacoo 3. 359:1354–1356, 04 2005.

[43] X. Dai, G. Kotliar, and Z. Fang. The Orbital Selective Mott Transition in a Three Band Hubbard model: a Slave Boson Mean Field Study. *arXiv:cond-mat/0611075*, November 2006.

[44] Luca de' Medici, S. R. Hassan, Massimo Capone, and Xi Dai. Orbital-selective mott transition out of band degeneracy lifting. *Phys. Rev. Lett.*, 102:126401, Mar 2009.

[45] A. Georges, L. de Medici, and J. Mravlje. Strong Correlations from Hund's Coupling. *Annual Review of Condensed Matter Physics*, 4:137–178, April 2013.

[46] Olle Gunnarsson, Erik Koch, and Richard M. Martin. Mott transition in degenerate hubbard models: Application to doped fullerenes. *Phys. Rev. B*, 54:R11026–R11029, Oct 1996.

[47] S. Florens, A. Georges, G. Kotliar, and O. Parcollet. Mott transition at large orbital degeneracy: Dynamical mean-field theory. *Phys. Rev. B*, 66:205102, Nov 2002.

[48] J. Schlipf, M. Jarrell, P. G. J. van Dongen, N. Blümer, S. Kehrein, Th. Pruschke, and D. Vollhardt. Absence of hysteresis at the mott-hubbard metal-insulator transition in infinite dimensions. *Phys. Rev. Lett.*, 82:4890–4893, Jun 1999.

[49] K. Inaba, A. Koga, S.-i. Suga, and N. Kawakami. Phase Diagram of Orbital-Selective Mott Transitions at Finite Temperatures. *Journal of the Physical Society of Japan*, 74:2393–2396, September 2005.

[50] A. Weichselbaum. Non-abelian symmetries in tensor networks: A quantum symmetry space approach. *Annals of Physics*, 327:2972–3047, December 2012.

[51] A. Weichselbaum and J. von Delft. Sum-rule conserving spectral functions from the numerical renormalization group. *Physical Review Letters*, 99(7):076402, August 2007.

[52] K. M. Stadler, Z. P. Yin, J. von Delft, G. Kotliar, and A. Weichselbaum. Dynamical mean-field theory plus numerical renormalization-group study of spin-orbital separation in a three-band hund metal. *Phys. Rev. Lett.*, 115:136401, Sep 2015.

[53] Emanuel Gull, Andrew J. Millis, Alexander I. Lichtenstein, Alexey N. Rubtsov, Matthias Troyer, and Philipp Werner. Continuous-time monte carlo methods for quantum impurity models. *Rev. Mod. Phys.*, 83:349–404, May 2011.

[54] M. J. Rozenberg, R. Chitra, and G. Kotliar. Finite temperature mott transition in the hubbard model in infinite dimensions. *Physical Review Letters*, 83:3498–3501, October 1999.

[55] G. Kotliar, E. Lange, and M. J. Rozenberg. Landau theory of the finite temperature mott transition. *Physical Review Letters*, 84:5180–5183, May 2000.

[56] Seung-Sup B. Lee, Jan von Delft, and Andreas Weichselbaum. Doublon-holon origin of the subpeaks at the hubbard band edges. *Phys. Rev. Lett.*, 119:236402, Dec 2017.

[57] Rong Yu and Qimiao Si. Mott transition in multiorbital models for iron pnictides. *Phys. Rev. B*, 84:235115, Dec 2011.

[58] Luca de' Medici. Hund's coupling and its key role in tuning multiorbital correlations. *Phys. Rev. B*, 83:205112, May 2011.

[59] Camille Aron and Gabriel Kotliar. Analytic theory of hund's metals: A renormalization group perspective. *Phys. Rev. B*, 91:041110, Jan 2015.

[60] S. Florens, A. Georges, G. Kotliar, and O. Parcollet. Mott transition at large orbital degeneracy: Dynamical mean-field theory. 66(20):205102, November 2002.

[61] Y. Ōno, M. Potthoff, and R. Bulla. Mott transitions in correlated electron systems with orbital degrees of freedom. *Phys. Rev. B*, 67:035119, Jan 2003.

[62] Li Huang, Liang Du, and Xi Dai. Complete phase diagram for three-band hubbard model with orbital degeneracy lifted by crystal field splitting. *Phys. Rev. B*, 86:035150, Jul 2012.

[63] F. Aryasetiawan and O. Gunnarsson. The GW method. *Reports on Progress in Physics*, 61:237–312, March 1998.

[64] Richard M. Martin. *Electronic Structure: Basic Theory and Practical Methods*. Cambridge University Press, 2008.

[65] P. G. J. van Dongen, F. Gebhard, and D. Vollhardt. Variational evaluation of correlation functions for lattice electrons in high dimensions. *Zeitschrift für Physik B Condensed Matter*, 76,77(2):199–210, 1989.